https://doi.org/10.1016/j.engfracmech.2022.108583

Effect of temperature variation on the plate-end debonding of FRP-strengthened steel beams: coupled mixed-mode cohesive zone modeling

Dong Guo[1], Hao Zhou[2], Hua-Ping Wang[3] & Jian-Guo Dai[4]*

1. PhD Candidate, Department of Civil and Environmental Engineering, The Hong Kong Polytechnic University, Hong Kong, China. (Email: dong.ce.guo@connect.polyu.hk)
2. Assistant Professor, School of Civil Engineering, Central South University, China. (Email: hao.zhou@csu.edu.cn)
3. Associate Professor, School of Civil Engineering and Mechanics, Lanzhou University, China. (Email: wanghuaping1128@sina.cn)
4. Professor, Professor, Department of Civil and Environmental Engineering, The Hong Kong Polytechnic University, Hong Kong, China. (Corresponding author, Email: cejgdai@polyu.edu.hk)

Abstract: Fiber-reinforced polymer (FRP) strengthened steel beams may experience significant temperature variation during their service life. Because of the different coefficients of thermal expansion (CTEs) of FRP and steel materials, thermal stresses can be generated by temperature variation at the FRP-to-steel interface and consequently influence the plate-end debonding mechanism. Therefore, an accurate prediction of the debonding failure of FRP-strengthened steel beams under combined mechanical and thermal loading is of great importance for the strengthening design. This paper proposes a closed-form analytical solution based on a coupled mixed-mode cohesive zone model (CZM) (i.e., with the consideration of Mode-I and Mode-II mixity), to analyze the effect of thermal stress on the debonding failure of FRP-strengthened steel beams. An excellent agreement has been achieved between the analytical solution and the finite element (FE) modeling in terms of interfacial full-range debonding behavior. Further parametric studies were conducted and indicated that the thermal stresses induced by elevated temperatures tend to reduce the plate-end debonding load and such effect becomes more significant when a thicker FRP plate is adopted.

Keywords: Fiber-reinforced polymer; steel beam; thermal effect; plate-end debonding; coupled mixed-mode analysis; cohesive zone model (CZM)

Nomenclature

a	distance between the FRP plate end and the support
A_1, A_2	sectional area of the steel beam and FRP plate
b_1, b_2	width of the steel beam and bonded FRP plate
d	single scalar damage variable in the coupled mixed-mode cohesive zone modeling (CZM)
E_1, E_2	elastic modulus of the steel beam and FRP plate
F	applied mechanical loading
F_{sof}	mechanical loading at onset of softening
G_I, G_{II}	interfacial fracture energy in normal and shear directions, respectively, under mixed-mode loading
G_{Ic}, G_{IIc}	critical interfacial fracture energy in normal and shear direction, respectively, under single mode loading
K_T, K_N	interfacial shear and normal stiffness, respectively
$K_T^{'}, K_N^{'}$	slope of the softening branch in shear and normal direction, respectively.
$K_{Tm}^{'}, K_{Nm}^{'}$	slope of the softening branch in shear and normal direction in mixed-mode analysis.
$K_{T,eff}^{'}$	slope of the softening branch of the ‘effective tangential CZ law’ in mixed-mode analysis
M_T	bending moment acting on the FRP-strengthened steel beam
M_1, M_2	bending moment applied on the steel beam and FRP plate, respectively
N_1, N_2	axial force applied on the steel beam and FRP plate, respectively
ΔT	temperature variation
l	half length of the FRP plate
R	ratio of the bending stiffness between two adhrends
t_a	thickness of the adhesive layer
I_1, I_2	second moment of inertia of the steel beam and FRP plate, respectively.
V_T	shear force acting on the FRP-strengthened beam
u_1, u_2	axial deformation at the tension soffit of the steel beam and top of the FRP plate, respectively
V_1, V_2	shear force applied on steel beam and FRP plate

x	distance from end of the FRP plate
$\bar{x}$	length of the softening region in *E-S* stage
y_1	distance between the neutral axis to the tension soffit of the steel beam
y_2	distance between the neutral axis to the top of the FRP plate
α	principle value of power in the mixed-mode fracture criterion
α_1, α_2	thermal expansion ratio of the steel beam and FRP plate, respectively
γ	displacement-based mode-mixity ratio
$\gamma^e, \gamma^{es}, \gamma^{deb}$	mode-mixity ratio in elastic stage, elastic-softening stage and debonding load, respectively
δ_t, δ_n	relative displacement in shear (interfacial slip) and normal direction (interfacial separation), respectively
δ_t^0, δ_n^0	interfacial slip and separation at peak stress, respectively
δ_t^f, δ_n^f	interfacial slip and separation at debonding, respectively, in single mode analysis
δ_t^{es}	distribution of interfacial slip in elastic-softening stage
δ_m	interfacial mixed-mode relative displacement
δ_m^0, δ_m^f	interfacial mixed-mode deformation at peak stress and debonding
$\delta_{tm}^0, \delta_{tm}^f$	interfacial slip at onset of softening and debonding, respectively, in mixed-mode analysis
$\delta_{nm}^0, \delta_{nm}^f$	interfacial separation at onset of softening and debonding, respectively, in mixed-mode analysis
$\varepsilon_1, \varepsilon_2$	axial train at tension soffit of the steel beam and the top of the FRP plate, respectively
v_1, v_2	vertical displacement at tension soffit of the steel beam and top of the FRP plate, respectively
σ	interfacial normal stress
σ^e	interfacial normal stress in elastic stage
σ_p	peak normal stress
σ_{pm}	peak normal stress at onset of softening in mixed-mode analysis
τ	interfacial shear stress
τ^e	interfacial shear stress in elastic stage
τ_p	peak shear stress
τ_{pm}	peak shear stress at softening initiation in mixed-mode analysis
$\tau_{p,eff}$	peak shear stress of the 'effective tangential CZ law' in mixed-mode

analysis

φ_T, φ_N amplification coefficient of distributions of interfacial slip and separation, respectively, in coupled mixed-mode analysis

Introduction

FRP composites have gained popularity in strengthening and retrofitting existing steel structures due to their many advantages such as the high strength-to-weight ratio, excellent durability performance and easy installation [1]. Existing research has shown that the flexural capacity of externally bonded (EB) FRP-strengthened steel beams can be significantly improved [2-6]. The performance of an FRP-strengthened steel beam is largely determined by the effectiveness of stress transfer between the steel beam and the FRP plate. The dominant failure mode is the plate-end debonding [2, 6-9], in which an interfacial crack initiates at the plate end and develops rapidly until the full debonding of the FRP plate. The plate-end debonding is generally attributed to the high interfacial stress concentration in both the mode-II (i.e., tangential or shear) and mode-I (i.e., normal) directions of the interface. Therefore, an accurate prediction on the bond behavior of FRP-strengthened steel beam is of great importance in determining its strengthening performance.

Due to the seasonal and diurnal temperature change, the service temperature of an FRP-strengthened steel beam could be changed from the installation temperature of FRP (i.e., the temperature at which the FRP is bonded to the steel). Such temperature change could lead to the thermal stress at the FRP-to-steel interface and consequently significantly affect the interfacial behavior and failure of FRP-strengthened steel beam. The thermal effect on the performance of FRP-strengthened steel beam was experimentally tested in previous studies at elevated temperatures [10-12] and decreased temperatures [13]. The test results showed that, when the strengthened beam fails in plate-end debonding, both the interfacial stress distributions and debonding load change as temperature varies. The effect of temperature variation can be considered from two aspects: 1) the temperature-dependent properties of the adhesive layer [14-16]; 2) the thermally induced interfacial stress [17, 18]. Specifically, as most of structural adhesives are ambient temperature cured ones, the mechanical properties of the adhesive layers are likely to be affected as the service temperature changes, especially when the temperature is close to or exceeds the glass transition temperature of the adhesive. As such, the bond behavior between the FRP and the substrate steel, including the interfacial stiffness, interfacial peak bond stress and interfacial fracture energy, could be deteriorated at elevated temperatures [15, 16, 19-26]. Meanwhile, the interfacial thermal stresses can be generated because of the discrepancy in coefficients of thermal expansions of steel and FRP materials. Depending on the direction of the initial thermal stress, the temperature variation could affect the bond strength between the FRP plate and steel substrate in different ways [17, 18, 27-29].

The thermal stress effect on the distributions of interfacial stresses in both longitudinal and normal directions to the FRP-to-steel interface in FRP-strengthened steel beams have been analyzed by closed-form solutions proposed by Deng et al. [30] and Stratford and Cadei [31], which was based on linear elastic assumption for the bond-slip/separation laws, i.e., the interfacial stresses are linearly proportional to the deformation of the adhesive layer. According to these analyses, the magnitude of interfacial stresses at both normal and shear directions generated by thermal loading was found to be comparable to that generated by mechanical loading. The plate-end debonding load of FRP-strengthened beam can be approximated by comparing the maximum interfacial normal and shear stresses with the corresponding tensile and shear strengths of the adhesive layer [30, 32]. However, such stress-based criterion may lead to underestimation of the plate-end debonding load due to the significant softening behavior of the interface, by which the interfacial fracture energy instead of the adhesive strength is a more dominant factor [1, 33-35].

To overcome the shortcomings of stress-based approach, cohesive zone model (CZM) has been adopted to analyze the interfacial behaviors of FRP-bonded concrete/steel joints [36] and FRP-strengthened concrete/steel beams [37, 38] subjected to mechanical loading only. In these models, the interfacial debonding is assumed to occur when the critical interfacial energy release rate is reached. Based on the cohesive zone model, some analytical solutions have been proposed to consider the effect of combined mechanical and thermal loading on the full-range bond behaviors of FRP-bonded steel joints [17, 18, 27, 29, 39] and curved FRP-concrete joints [28]. For FRP-bonded joints subjected to mode-II loading, it has been shown that the initial thermal stress induced by elevated temperatures improves the bond strength significantly. Similar enhancement in the intermediate crack-induced (IC) debonding load has also been observed in the FRP-retrofitted steel beam with precast notch at middle span [40]. In contrast, in FRP-strengthened steel beams, Guo et al. [41] found that the thermal stress induced by elevated temperature leads to reduced plate-end debonding load based on the assumption that the FRP-to-steel interface is subjected to Mode-II loading only. In reality, the Mode-I stress in the normal direction of the interface may have a comparable magnitude as that in the shear direction (i.e., Mode-II loading) in FRP-strengthened steel beams [30].

The coupled mixed-mode cohesive zone model, which considers the interaction of both mode-I and mode-II stresses on the onset of plate-end debonding was presented by Camanho et al. [42]. Since then, three typical criteria governing the interface failure, including quadratic failure criterion [43], power law criterion [44], and B-K criterion [45] were often adopted in analyzing the interfacial behaviors and predicting the debonding loads of FRP-strengthened steel beams in FE modeling [6, 46-48]. In addition, based on coupled mixed-mode CZM, De Lorenzis et al. [49] developed closed-form analytical solutions to predict the interfacial behavior of an FRP-strengthened steel beam under mechanical loading only, in which the quadratic failure criterion and power law criterion were utilized in predicting the onset of softening and debonding of the adhesive layer.

In view of the important effect of thermal stress on the plate-end debonding of the FRP-strengthened beam as well as the importance of coupled mode-I and mode-II analysis, this paper aims to develop a closed-form solution based on coupled mixed-mode failure theory to analyze the interfacial behaviors and plate-end debonding failure of FRP-strengthened steel beams subjected to combined mechanical loading and temperature variation.

Problem Definition and Assumptions

Fig. 1 illustrates a simply supported FRP-strengthened steel beam subjected to three-point bending and temperature variation. As shown in the figure, the flange width of the I-beam is b_1 and the distance from its neutral axis to the bottom is y_1. An FRP plate with a width of b_2 and a length of $2l$ is bonded to the tension soffit of the I-beam by adhesive layer with thickness of t_a. y_2 is the distance between the neutral axis to the top surface of the FRP plate. a is the distance from the plate end to the support. The second moment of inertia, sectional area, and the elastic modulus of the adherend are noted as I, A, E, with the subscripts '1' and '2' representing the beam and FRP plate respectively. Due to the symmetry of the simply supported beam, only half of the strengthened beam with the x axis originating from the end of the FRP plate, is analyzed in this study.

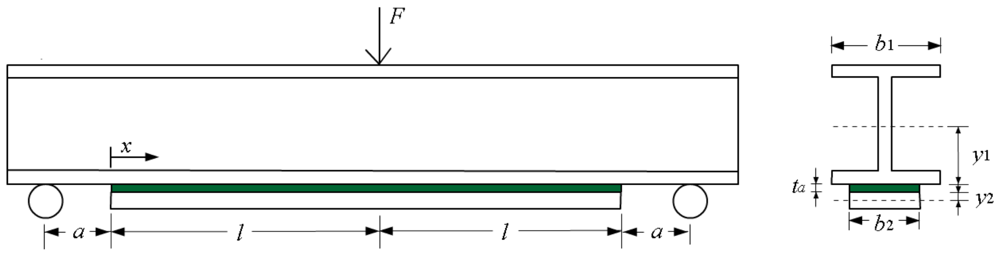

Fig. 1 Simply supported strengthened beam under three-point bending

To find a closed-form solution for predicting the interfacial behavior of the above FRP strengthened steel beam, several common assumptions are adopted in the present study:

1. Both the steel beam and the FRP plate are linearly elastic. The transverse shear deformation of the two adherends are ignored;
2. Magnitudes of interfacial shear and normal stresses are invariant across the thickness of the adhesive layer;
3. Sectional properties, the elastic moduli of steel beam and FRP plate are constant at varying temperatures;
4. The temperature variation and thermal deformation of the FRP-strengthened steel beam are uniformly distributed along axial direction.

Cohesive Zone Model

Before the introduction of coupled mixed-mode CZM analysis, the interfacial behavior under single mode CZM analysis is briefly introduced in this section.

Single Mode Interface Analysis

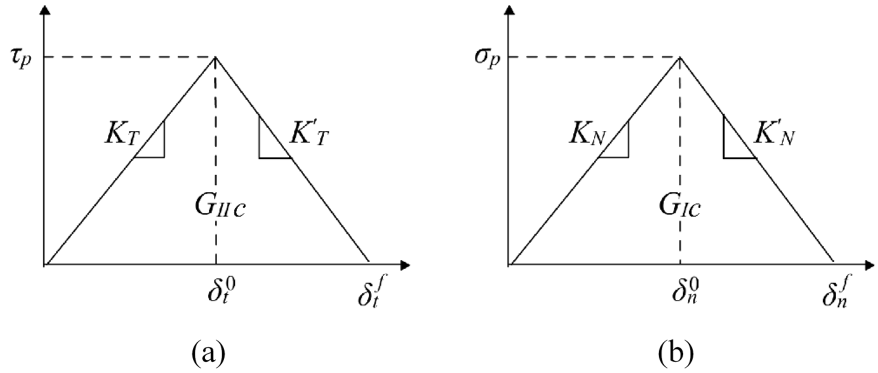

Fig. 2 illustrates the interfacial bond behavior between the steel substrate and FRP plate, including a bond-slip relationship under mode-II loading (**Fig.2a**) and a bond-separation relationship under mode-I loading (**Fig.2b**).

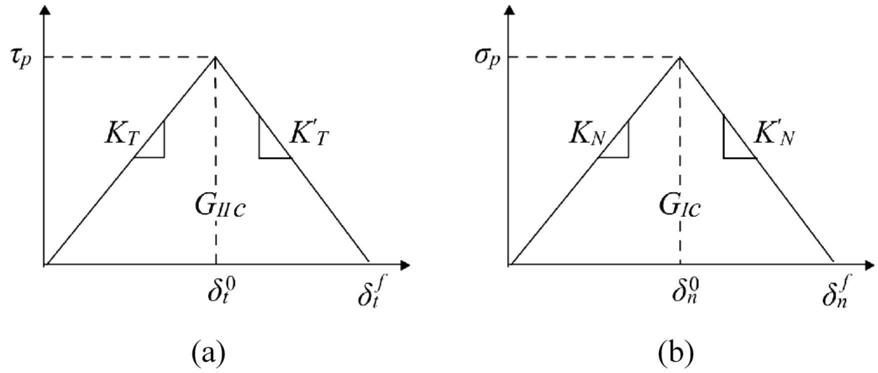

Fig. 2 Bond-slip/separation relationship in CZM: a) mode-II; b) mode-I.

Both the above two relationships are assumed to be bilinear and can be expressed as follows:

$$\tau = \begin{cases} K_T \delta_t & if\ \delta_t < \delta_t^0 \\ \tau_p - K_T'(\delta_t - \delta_t^0) & if\ \delta_t^0 < \delta_t < \delta_t^f \\ 0 & if\ \delta_t^f < \delta_t \end{cases}$$

$$\sigma = \begin{cases} K_N \delta_n & if\ \delta_n < \delta_n^0 \\ \sigma_p - K_N'(\delta_n - \delta_n^0) & if\ \delta_n^0 < \delta_n < \delta_n^f \\ 0 & if\ \delta_n^f < \delta_n \end{cases} \quad (1)$$

in which τ and σ represent the interfacial stress in shear and normal directions with subscript 'p' indicates the peak magnitude when softening initiates. δ is the interfacial deformation, with subscripts 't' and 'n' denoting the shear and normal directions, respectively. Superscripts '0' and 'f' represent the critical magnitude at onset of softening and debonding, respectively. K and K' are the slopes of the bilinear relationship in the elastic and softening branches, respectively, with the subscripts 'T' and 'N' indicating the tangential or normal direction, respectively.

The critical energy release rates, i.e., interfacial fracture energies under mode-I and mode-II (i.e., G_{IC}, G_{IIC}) loadings, respectively, are defined as the areas enclosed beneath the relationship as follows:

$$G_{IIC} = \frac{1}{2}\tau_p \delta_t^f \text{ and } G_{IC} = \frac{1}{2}\sigma_p \delta_n^f \tag{2}$$

Based on the bond-slip relationship in mode-II direction

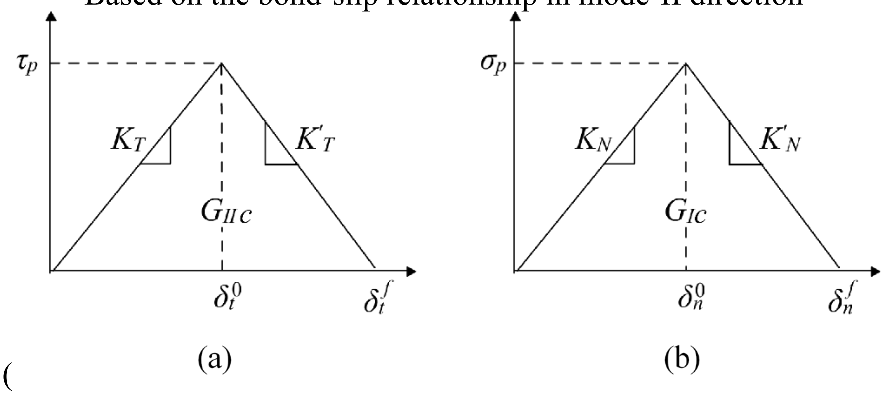

(Fig. 2a), the interfacial bond behavior in FRP-strengthened steel beam subjected to coupled mechanical loading and temperature variation has been analyzed by Guo et al. [41] on the assumption that only mode-II loading is exerted at the FRP-to-steel interface. **Fig. 3** shows the obtained typical distributions of shear stresses and slips along the interface, in which the interfacial shear stresses and slips are normalized by the peak shear stress (τ_p) and the corresponding slip (δ_t^0), respectively. The deformation process of the interface evolves from *E* stage to *E-S* stage as the load or temperature increase. During *E* stage, the interfacial shear stress/slip is larger near the plate end and increases with increasing the mechanical loading or temperature. After the peak shear stress (τ_p) is reached at the plate end, the deformation process evolves to the elastic-softening (*E-S*) stage. During this stage, the softening first starts at the plate end and extends to the mid span of the beam gradually. As the load/temperature increases, the interfacial shear stress near the plate end increases first (i.e., *E* stage) and then decreases once the interface enters the softening (i.e., *E-S* stage). In comparison, the interfacial slip increases monotonically in both E and E-S stage with increasing of the mechanical or thermal loading. Finally, plate-end debonding occurs when the interface enters into the elastic-softening-debonding (E-S-D) stage, i.e., the interfacial shear stress at the plate end decreases to zero and the interfacial slip increases to δ_t^f.

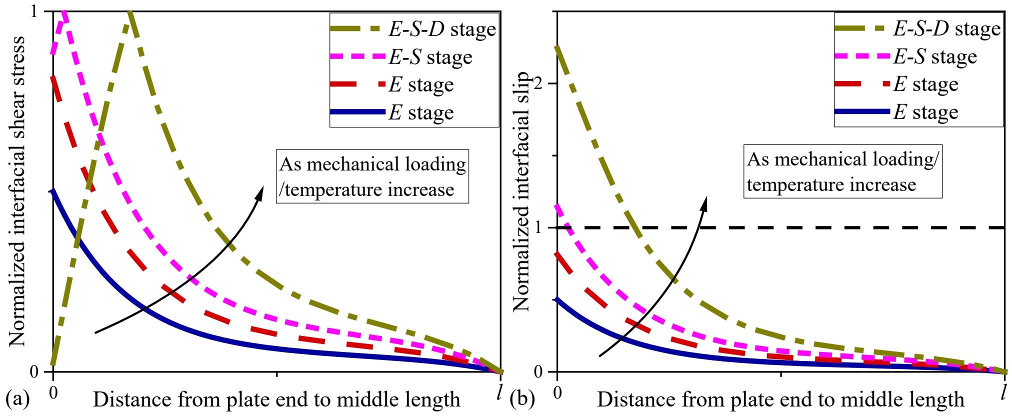

Fig. 3 Interfacial bond behavior in FRP-strengthened beam under increased mechanical or thermal loading: distributions of a) normalized interfacial shear stress; b) normalized interfacial slip.

It can be noted from **Fig. 3a**, as the load increases, both the increase and decrease of the interfacial shear stress can be observed at the plate end in E stage and E-S stage, respectively. But the interfacial slip increases monotonically with the increase of the applied mechanical or thermal loading (**Fig. 3b**). As such, it is easy to identify the deformation stage of the interface based on the magnitude of interfacial slip at the plate end [i.e., $\delta_t(0) < \delta_t^0$ in E stage; $\delta_t^0 < \delta_t(0) < \delta_t^f$ in E-S stage; $\delta_t(0) \geq \delta_t^f$ in E-S-D stage].

In addition, in single mode-II analysis, the length of softening region ($\bar{x}$) in E-S stage is an essential parameter, when determining the distribution of interfacial stresses. That is because it corresponds to the turning point of the bilinear bond-slip relationship (i.e., the peak shear stress point in **Fig. 2a**). The length of the softening region can be determined for a given load F and temperature variation ΔT as follows [41]:

$$\frac{F}{2} = \frac{\tau_p\{\tan(\lambda'\bar{x}) + r\coth[\lambda(l-\bar{x})]\} + \dfrac{m_3'\Delta T}{\lambda'\cos(\lambda'\bar{x})}}{\dfrac{m_1\sin(\lambda'\bar{x}) + \dfrac{m_2'a}{\lambda'}}{\cos(\lambda'\bar{x})} + m_1 r\dfrac{\cos[\lambda(l-\bar{x})]-1}{\sin[\lambda(l-\bar{x})]}} \tag{3}$$

where F is the applied mechanical load and ΔT is the temperature variation; λ, r, λ', m_3', m_1, m_2' are constants which can be calculated based on the inherent properties of the FRP plate and the steel beam [41].

It should be mentioned here that the above-presented bilinear bond-slip relationship has been most often adopted for describing the interfacial bond behavior of the FRP-to-steel interface under Mode-II loading. However, the parameters in the bond-slip relationship may be significantly different, in terms of interfacial shear stiffness, peak shear stress and interfacial fracture energy, when different types of glue are used [16, 22, 34, 50, 51]. When a ductile glue is used, the bond-slip relationship may change from a bilinear shape to a trapezoid shape [34, 50]. However, if the interfacial fracture energy is appropriately defined, it is usually assumed the shape of the softening part of the bond-slip relationship only influences the local bond stress distribution instead of the ultimate debonding load [18].

Coupled Mixed-Mode Cohesive Zone Model

Fig. 4 shows the interfacial bond-slip/separation relationships between the FRP plate and the steel beam in coupled mixed-mode analysis. It can be observed that, the bond strengths in both mode-I and mode-II directions are compromised in the coupled mixed-mode analysis. In the theoretical analysis, the bond behaviors in mode-I and mode-II directions are assumed to develop independently, following the reduced bond-slip/separation relationships shown in **Fig. 4**. The bond behaviors in both directions are only related when determining the parameters of the reduced bond-slip/separation relationships at onset of softening and debonding.

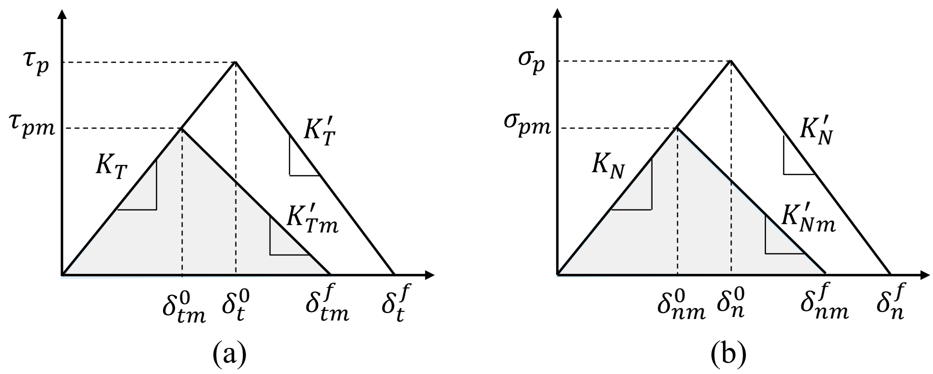

Fig. 4 Interfacial CZ laws: a) mode-II; b) mode-I.

Similar to the single mode-II analysis, the deformation stage of the interface can also be distinguished according to the mixed-mode interfacial deformation in the coupled mixed-mode analysis. The magnitude of mixed-mode deformation is defined as δ_m, which is the square root of the quadratic sum of relative displacements in both tangential (δ_t) and normal (δ_n) directions:

$$\delta_m = \sqrt{{\delta_t}^2 + \langle \delta_n \rangle^2} \tag{4}$$

where the Macaulay bracket ($\langle \quad \rangle$) indicates that the compressive deformation (i.e., $\delta_n < 0$) in normal direction does not generate any damage to the interface (also adopted in Eq. 7).

In addition, when $\delta_n > 0$, the displacement-based mode-mixity ratio is defined as,

$$\gamma = \frac{\delta_t}{\delta_n} \tag{5}$$

Considering that the distributions of interfacial slip and separation along the bondline [i.e., $\delta_t(x)$ and $\delta_n(x)$] change with the applied mechanical loading, γ is function of x and F.

With Eqs. (4) and (5), the tangential and normal components of the relative displacement can be expressed as follows:

$$\delta_t = \frac{\gamma \delta_m}{\sqrt{1+\gamma^2}}; \ \delta_n = \frac{\delta_m}{\sqrt{1+\gamma^2}} \tag{6}$$

Criterion for Onset of Softening

The initiation of softening is defined by the quadratic stress failure criterion, as follows:

$$(\frac{\tau}{\tau_p})^2 + (\frac{\langle\sigma\rangle}{\sigma_p})^2 = 1 \tag{7}$$

To satisfy this equation, the corresponding maximum interfacial stresses in both shear and normal directions, which are termed as τ_{pm} and σ_{pm}, should be less than or at maximum equal to the interfacial strength in single-mode conditions (i.e., τ_p and σ_p).

Substituting the mixed-mode displacement at onset of softening (δ_m^0) into Eq. (6) yields

$$\delta_{tm}^0 = \frac{\gamma\delta_m^0}{\sqrt{1+\gamma^2}};\ \delta_{nm}^0 = \frac{\delta_m^0}{\sqrt{1+\gamma^2}} \tag{8}$$

where δ_{tm}^0 and δ_{nm}^0 are the interfacial slip and separation at onset of softening in mixed-mode analysis, respectively.

Correspondingly, the mixed-mode displacement at the onset of softening (δ_m^0) can be calculated by δ_{tm}^0 and δ_{nm}^0. By considering the bond-slip/separation relationship in elastic stage (Eq. 1) and substituting Eq. (8) into Eq. (7), δ_m^0 can be expressed as

$$\delta_m^0 = \begin{cases} \delta_t^0\delta_n^0\sqrt{\frac{1+\gamma^2}{{\delta_t^0}^2+\gamma^2}} & if\ \delta_n^0 > 0 \\ \delta_t^0 & if\ \delta_n^0 \le 0 \end{cases} \tag{9}$$

Criterion for Onset of Debonding

The criterion for the initiation and propagation of debonding was assumed to follow the power-law mixed-mode fracture criterion:

$$(\frac{G_I}{G_{Ic}})^\alpha + (\frac{G_{II}}{G_{IIc}})^\alpha = 1 \tag{10}$$

where G_{Ic} and G_{IIc} are the critical fracture energies in single mode-I and mode-II conditions, respectively (Eq. 2). While the power factor (α) is taken as 1 as suggested in previous studies [6, 47, 49].

When Eq. (10) is satisfied,

$$G_I = \frac{1}{2}\tau_{pm}\delta_{tm}^f \text{ and } G_{II} = \frac{1}{2}\sigma_{pm}\delta_{nm}^f \quad (11)$$

where δ_{tm}^f and δ_{nm}^f are the interfacial displacements in shear and normal directions in coupled mixed-mode analysis when debonding occurs (**Fig. 4**). In an analogy to Eq. (6), δ_{tm}^f and δ_{nm}^f can be expressed as functions of δ_m^f and γ, i.e.,

$$\delta_{tm}^f = \frac{\gamma\delta_m^f}{\sqrt{1+\gamma^2}};\ \delta_{nm}^f = \frac{\delta_m^f}{\sqrt{1+\gamma^2}} \quad (12)$$

By substituting Eqs. (11) and (12) into Eq. (10), mixed-mode displacement at onset of debonding (δ_m^f) can be obtained as

$$\delta_m^f = \frac{2(1+\gamma^2)}{\delta_m^0}[\left(\frac{K_N}{G_{Ic}}\right)^\alpha + \left(\frac{\gamma^2 K_T}{G_{IIc}}\right)^\alpha]^{-1/\alpha} \quad (13)$$

From Eqs. (9) and (13), it can be seen that for given interfacial bond-slip/separation relationships, the magnitudes of δ_m^0 and δ_m^f only depend on the mode-mixity ratio (γ).

Similar to the mode-II analysis, the deformation stage of the interface can be distinguished by the mixed-mode deformation at plate end [$\delta_m(0)$]. When $\delta_m(0)$ is smaller than δ_m^0, the interface is in *E* stage. Then it evolves to *E-S* stage, when $\delta_m(0)$ is greater than δ_m^0 and smaller than δ_m^f. Finally, the debonding occurs while $\delta_m(0)$ increases to δ_m^f.

Cohesive Zone Model at Softening Stage

In *E-S* stage, the interface near plate end enters the softening stage, thus the slopes of the softening branches in the bond-slip/separation relationships can be computed as follows:

$$K'_{Tm} = \frac{K_T\delta_{tm}^0}{\delta_{tm}^f - \delta_{tm}^0};\ K'_{Nm} = \frac{K_N\delta_{nm}^0}{\delta_{nm}^f - \delta_{nm}^0} \quad (14)$$

And the following definition is introduced

$$r_m = \sqrt{\frac{K'_{Tm}}{K_T}} \quad (15)$$

And r_m tends to be a constant value when the mode-mixity ratio (γ) is sufficiently large

[49].

In coupled mixed-mode analysis, the damage evolution in softening region is described through a single scalar damage variable (d), which is defined as follows,

$$d = \frac{\delta_m^f(\delta_m - \delta_m^0)}{\delta_m(\delta_m^f - \delta_m^0)} \tag{16}$$

Thus, the interfacial stresses in the entire deformation stages can be calculated as:

$$\tau = \begin{cases} K_T\delta_t & \delta_m \leq \delta_m^0 \\ (1-d)K_T\delta_t & \delta_m^0 \leq \delta_m \leq \delta_m^f \\ 0 & \delta_m^f \leq \delta_m \end{cases} \tag{17}$$

$$\sigma = \begin{cases} K_N\delta_n & \delta_m \leq \delta_m^0 \\ (1-d)K_N\delta_n & \delta_m^0 \leq \delta_m \leq \delta_m^f \\ 0 & \delta_m^f \leq \delta_m \end{cases} \tag{18}$$

Interfacial Behavior at Elastic Stage

In this section, an analytical solution is proposed based on elastic mechanics theory to derive the interfacial behavior in *E* stage, in which the thermal deformation of both adherends and the interfacial thermal stress is considered.

Interfacial Shear Stress

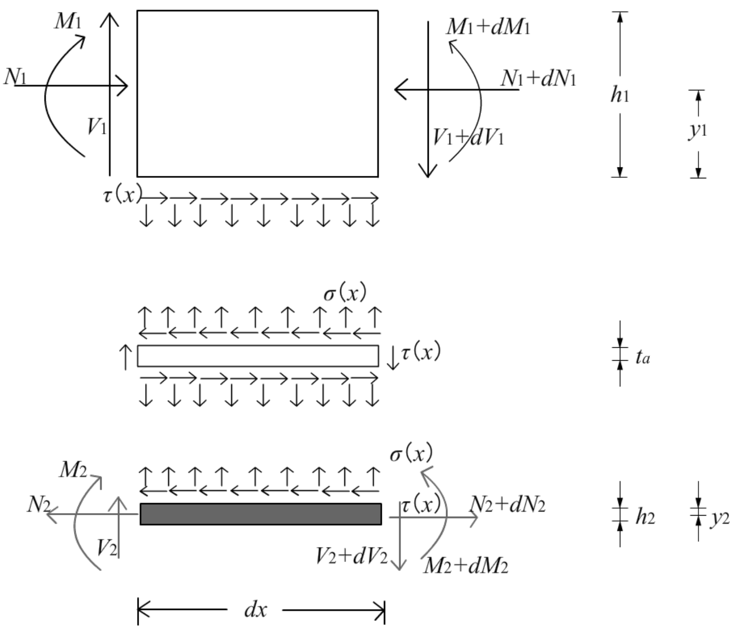

Fig. 5 Differential element of the strengthened beam

Fig. 5 illustrates a differential segment of the FRP-strengthened steel beam with a length of dx. Both adherends are subjected to axial force, shear force, bending moment and interfacial stresses in shear and normal directions. And the following equilibrium equations can be established.

$$\frac{dN_1(x)}{dx} = \tau(x)b_2 \qquad \frac{dN_2(x)}{dx} = \tau(x)b_2 \tag{19}$$

$$N_1 = N_2 \tag{20}$$

$$\frac{dM_1(x)}{dx} = V_1(x) - \tau(x)b_2y_1 \qquad \frac{dM_2(x)}{dx} = V_2(x) - \tau(x)b_2y_2 \tag{21}$$

where M, V, N are the bending moment, axial and shear force sustained by each adherend, with subscript '1' and '2' representing the steel beam and FRP plate.

For the FRP-strengthened steel beam illustrated in **Fig. 1**, the overall moment equilibrium of the differential element in the strengthened beam yields,

$$\frac{dM_T(x)}{dx} = V_T(x) = \frac{F}{2} \tag{22}$$

$M_T(x)$ and $V_T(x)$ are the bending moment and shear force acting on the FRP-strengthened beam at x. Considering the flexural stiffness of both adherends, the moment equilibrium can be expressed as follows:

$$M_T = M_1 + M_2 + N_1(y_1 + y_2 + t_a) \tag{23}$$

To uncouple the differential equations, the curvatures of the FRP plate and steel beam are assumed to be equal in deriving the distribution of the interfacial shear stress [52]. As such, the relationship of moment in both adherends can be expressed as:

$$M_1 = RM_2; \quad R = \frac{E_1 I_1}{E_2 I_2} \tag{24}$$

By substituting Eq. (24) into Eq. (23), the bending moment acting on the steel beam and the FRP plate can be expressed as function of M_T and the axial force N_1:

$$M_1 = \frac{R}{R+1} M_T - \frac{R}{R+1} N_1(y_1 + y_2 + t_a) \tag{25}$$

$$M_2 = \frac{1}{R+1} M_T - \frac{1}{R+1} N_1(y_1 + y_2 + t_a) \tag{26}$$

For a temperature change as ΔT, the strain on tension soffit of the steel beam (ε_1) and top of FRP plate (ε_2) can be expressed as follows:

$$\varepsilon_1(x) = \frac{du_1}{dx} = \frac{y_1}{E_1 I_1} M_1(x) - \frac{1}{E_1 A_1} N_1(x) + \alpha_1 \Delta T \tag{27}$$

$$\varepsilon_2(x) = \frac{du_2}{dx} = -\frac{y_2}{E_2 I_2} M_2(x) + \frac{1}{E_2 A_2} N_2(x) + \alpha_2 \Delta T \tag{28}$$

where α_1 and α_2 are the thermal expansion coefficients of the steel beam and the FRP, respectively.

The interfacial slip in tangential direction can be expressed as:

$$\delta_t(x) = u_2(x) - u_1(x) \tag{29}$$

In *E* stage, the interfacial shear stress can be obtained by substituting Eq. (29) into Eq. (1) and described as:

$$\tau^e(x) = K_T[u_2(x) - u_1(x)] \tag{30}$$

where superscripts ‘e’ indicates the *E* stage.

Differentiating Eq. (30) twice and substituting the differentiation of Eqs. (27) and (28) yield:

$$\frac{d^2\tau^e(x)}{dx^2} = K_T[\frac{y_1}{E_1I_1}\frac{dM_1(x)}{dx} + \frac{y_2}{E_2I_2}\frac{dM_2(x)}{dx} - \frac{1}{E_1A_1}\frac{dN_1(x)}{dx} - \frac{1}{E_2A_2}\frac{dN_2(x)}{dx}] \quad (31)$$

Furthermore, substituting Eqs. (25) and (26) into the above equation gives the following governing equation for the distribution of interfacial shear stress:

$$\frac{d^2\tau^e(x)}{dx^2} - K_Tb_2[\frac{(y_1+y_2)(y_1+y_2+t_a)}{E_1I_1+E_2I_2} + \frac{1}{E_1A_1} + \frac{1}{E_2A_2}]\tau^e(x) + K_T\left(\frac{y_1+y_2}{E_1I_1+E_2I_2}\right)V_T(x) = 0 \quad (32)$$

The general solutions of Eq. (32) is given by

$$\tau^e(x) = B_1\cosh(\lambda x) + B_2\sinh(\lambda x) + m_1\frac{F}{2} \quad (33)$$

where $\lambda^2 = K_Tb_2[\frac{(y_1+y_2)(y_1+y_2+t_a)}{E_1I_1+E_2I_2} + \frac{1}{E_1A_1} + \frac{1}{E_2A_2}]$ and $m_1 = \frac{K_T}{\lambda^2}\left(\frac{y_1+y_2}{E_1I_1+E_2I_2}\right)$.

B_1 and B_2 are the integration constants and can be calculated by applying suitable boundary conditions.

At the plate end ($x = 0$), the axial force of either the steel beam or the FRP plate is zero. And the moment resisted by FRP plate is zero at the plate end. As such, the following boundary conditions can be obtained as follows,

$$N_1(0) = 0;\ N_2(0) = 0;\ M_2(0) = 0 \quad (34)$$

Substituting Eqs. (27) and (28) into differentiation of Eq. (30) obtains

$$\left.\frac{d\tau^e(x)}{dx}\right|_{x=0} = K_T[-\frac{y_2}{E_2I_2}M_2(x) - \frac{y_1}{E_1I_1}M_1(x) + \frac{1}{E_2A_2}N_2(x) + \frac{1}{E_1A_1}N_1(x) + (\alpha_2-\alpha_1)\Delta T)] \quad (35)$$

Furthermore, by applying the preceding boundary conditions, Eq. (35) can be derived as:

$$\left.\frac{d\tau^e(x)}{dx}\right|_{x=0} = -m_2M_1(0) + K_T(\alpha_2-\alpha_1)\Delta T \quad (36)$$

where, $m_2 = \frac{K_Ty_1}{E_1I_1}$, $M_1(0) = M_T(0) = \frac{Fa}{2}$.

By comparing the first derivative of (33) with Eq. (36), B_2 can be determined as

$$B_2 = \frac{1}{\lambda}[-\frac{m_2a}{2}F + K_T(\alpha_2-\alpha_1)\Delta T] \quad (37)$$

Due to the symmetry of the FRP-strengthened steel beam, the interfacial shear stress at mid-span is zero [i.e., $\tau^e(l) = 0$]. Then B_1 can be determined as follows:

$$B_1 = \frac{1}{2}[\frac{m_2 a}{\lambda}\tanh(\lambda l) - \frac{m_1}{\cosh(\lambda l)}]F - \frac{\tanh(\lambda l)}{\lambda}K_T(\alpha_2 - \alpha_1)\Delta T \tag{38}$$

Interfacial Normal Stress

Similar to Eq. (30), the interfacial normal stress in *E* stage can be expressed as:

$$\sigma^e(x) = K_N[v_2(x) - v_1(x)] \tag{39}$$

where $v_1(x)$ and $v_2(x)$ are the vertical components of the displacements at the bottom of the steel beam and top of the FRP plate, respectively. And the difference between $v_1(x)$ and $v_2(x)$ represents the interfacial separation.

The vertical shear force applied on each adherend is balanced by interfacial normal stress.

$$\frac{dV_1(x)}{dx} = -b_2\sigma(x); \frac{dV_2(x)}{dx} = b_2\sigma(x) \tag{40}$$

According to the Euler-Bernoulli beam theory,

$$\frac{d^2v_1(x)}{dx^2} = -\frac{1}{E_1I_1}M_1(x); \frac{d^2v_2(x)}{dx^2} = -\frac{1}{E_2I_2}M_2(x) \tag{41}$$

Differentiate Eq. (39) four times and substituting the twice derivation of Eq. (41), the following equation can be obtained:

$$\frac{d^4\sigma^e(x)}{dx^4} = K_N[\frac{1}{E_1I_1}\frac{d^2M_1(x)}{dx^2} - \frac{1}{E_2I_2}\frac{d^2M_2(x)}{dx^2}] \tag{42}$$

By substituting the differentiations of Eqs. (21) and (40), the final governing differential equation of normal stress is given as:

$$\frac{d^4\sigma^e(x)}{dx^4} - K_Nb_2\left(\frac{1}{E_1I_1} + \frac{1}{E_2I_2}\right)\sigma^e(x) + K_Nb_2\left(\frac{y_1}{E_1I_1} - \frac{y_2}{E_2I_2}\right)\frac{d\tau^e(x)}{dx} = 0 \tag{43}$$

With $d^5\tau^e(x)/dx^5$ neglected [52], the general solution to this four-order differential equation is

$$\sigma^e(x) = e^{-\beta x}[C_1\cos(\beta x) + C_2\sin(\beta x)] + e^{\beta x}[C_3\cos(\beta x) + C_4\sin(\beta x)] - n_1\frac{d\tau^e(x)}{dx} \tag{44}$$

Where $\beta = \sqrt[4]{\frac{K_N b_2}{4}\left(\frac{1}{E_1 I_1} + \frac{1}{E_2 I_2}\right)}$, $n_1 = \frac{y_1 E_2 I_2 - y_2 E_1 I_1}{E_1 I_1 + E_2 I_2}$, $n_3 = K_N b_2 [\frac{y_1}{E_1 I_1} - \frac{y_2}{E_2 I_2}]$.

C_1 to C_4 are integrity constants. By noting that when $x \to \infty$, $\sigma \to 0$, therefore, C_3, C_4 are eliminated.

Then Eq. (44) evolves to the following simple form:

$$\sigma^e(x) = e^{-\beta x}[C_1 \cos(\beta x) + C_2 \sin(\beta x)] - n_1 \lambda [B_1 \sinh(\lambda x) + B_2 \cosh(\lambda x)] \tag{45}$$

Substituting Eq. (41) into the second derivative of Eq. (39) and applying the boundary condition at plate end [i.e., $M_1(0) = Fa$] lead to

$$\left.\frac{d^2 \sigma^e(x)}{dx^2}\right|_{x=0} = K_N \left[\frac{1}{E_1 I_1} M_1(0) - \frac{1}{E_2 I_2} M_2(0)\right] = \frac{K_N a}{2 E_1 I_1} F \tag{46}$$

Substituting Eq. (41) into the third derivative of Eq. (39) yields

$$\left.\frac{d^3 \sigma^e(x)}{dx^3}\right|_{x=0} = K_N [\frac{1}{E_1 I_1} V_1(0) + \frac{1}{E_2 I_2} V_2(0)] + K_N b_2 \left(\frac{y_1}{E_1 I_1} - \frac{y_2}{E_2 I_2}\right) \tau^e(0) \tag{47}$$

Considering the boundary condition of shear force at the plate end [i.e., $\mathrm{V}_2(0) = 0; \mathrm{V}_1(0) = \mathrm{V}_\mathrm{T}(0) = \frac{\mathrm{F}}{2}$], the above equation can be rewritten as follows:

$$\left.\frac{d^3 \sigma^e(x)}{dx^3}\right|_{x=0} = \frac{K_N}{E_1 I_1} \frac{F}{2} + n_3 \left(B_1 + m_1 \frac{F}{2}\right) \tag{48}$$

where

$$n_3 = K_N b_2 \left(\frac{y_1}{E_1 I_1} - \frac{y_2}{E_2 I_2}\right) \tag{49}$$

By substituting second and third derivative of Eq. (45) into Eqs. (46) and (48), C_1 and C_2 can be determined as follows:

$$C_1 = \frac{K_N}{4\beta^3} \frac{F}{E_1 I_1} (1 + \beta a) + \frac{n_1 \lambda^3}{2\beta^3} (\lambda B_1 + \beta B_2) - \frac{n_3}{2\beta^3} (B_1 + m_1 \frac{F}{2}) \tag{50}$$

$$C_2 = -\frac{K_N}{4\beta^2} \frac{Fa}{E_1 I_1} - \frac{n_1}{2\beta^2} \lambda^3 B_2 \tag{51}$$

With the above constants, the distributions of relative displacements in both shear and normal directions along the bondline in *E* stage can be expressed as

$$\delta_t^e(x) = \frac{1}{K_T}[B_1 \cosh(\lambda x) + B_2 \sinh(\lambda x) + m_1 \frac{F}{2}] \tag{52}$$

$$\delta_n^e(x) = \frac{1}{K_N}\{e^{-\beta x}[C_1 \cos(\beta x) + C_2 \sin(\beta x)] - n_1 \lambda [B_1 \sinh(\lambda x) + B_2 \cosh(\lambda x)]\} \tag{53}$$

The Mechanical Load at Onset of Softening

According to the interfacial behavior of FRP-strengthened steel beam in *E* stage (**Fig. 3a**), the maximum interfacial stresses is located at the plate end. Consequently, the softening and debonding initiate at the plate end. Using Eqs. (33) and (45), the magnitude of interfacial stresses at softening initiation ($F = F_{sof}$) at the plate end ($x = 0$) can be expressed as

$$\tau^e(0) = B_1 + m_1 \frac{F_{sof}}{2} \qquad \sigma^e(0) = C_1 - n_1 \lambda B_2 \tag{54}$$

Substituting Eq. (54) into Eq. (7), and considering a positive σ^e at the plate end gives,

$$(\frac{B_1 + m_1 \frac{F_{sof}}{2}}{\tau_p})^2 + (\frac{C_1 - n_1 \lambda B_2}{\sigma_p})^2 = 1 \tag{55}$$

As B_1, B_2, C_1 are functions of F and ΔT, for a given temperature variation ΔT, the mechanical loading at onset of softening (F_{sof}) can be obtained by solving Eq. (55).

Interfacial Behavior in Elastic-Softening stage

After interfacial softening occurs at the plate end, the interfacial behavior should be interpreted by the softening branches in the mixed-mode CZ law in both mode-I and mode-II directions. In coupled mixed-mode analysis, the parameters in softening branches (i.e., peak stresses and slopes of softening branches) are changed compared with the single mode analysis (**Fig. 4**). And these parameters are dependent on the coupling and mutual influence of the interfacial displacements in both mode-I and mode-II directions.

In De Lorenzis et al.'s analysis [49], an 'effective tangential cohesive zone (CZ) law' was proposed for describing the interfacial bond behavior in mode-II direction in *E-S* stage. By adopting the 'effective tangential CZ law', the distributions of interfacial shear stress and magnitude of the single scalar damage variable (d) can be determined based on mode-II analysis. Then the interfacial bond behavior in mode-I direction can be obtained based on Eq. (18). The proposed analytical solution in this paper generally follows this method.

Effective Tangential Cohesive Zone Law

Fig. 6 shows the 'effective tangential CZ law' used in the mixed-mode analysis. The effect of Mode I loading (i.e., the interfacial normal stress and separation) on the Mode II bond behavior in the coupled mixed-mode analysis is considered by decreasing the peak shear stress ($\tau_{p,eff}$) and varied slope of softening branch ($K'_{T,eff}$) in the bond-slip relationship. In the 'effective tangential CZ law', the bond-slip relationship in softening branch is still assumed to be linear. The softening branch is determined by the instantaneous bond-slip data at two points, including the point with the peak shear stress at $x = \bar{x}$ [i.e., $\delta_t^{es}(\bar{x})$, $\tau_{p,eff}$] and the point with maximum shear slip at $x = 0$ [i.e., $\delta_t^{es}(0)$, $\tau_t^{es}(0)$]. Considering that these parameters change as the variation of applied mechanical loading in *E-S* stage, the 'effective tangential CZ law' also varies at different levels of thermal and mechanical loading.

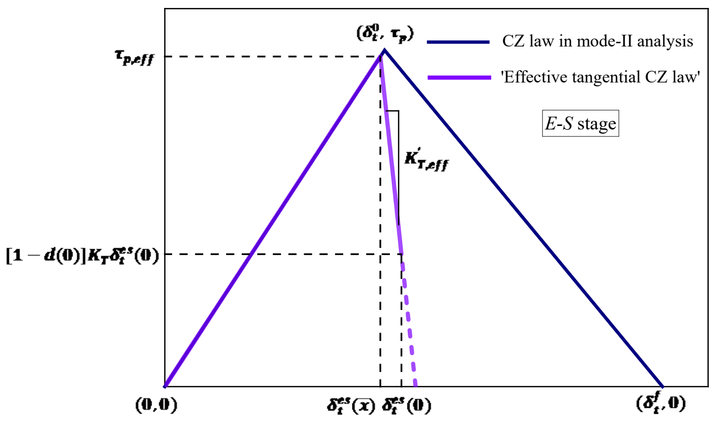

Fig. 6 'Effective tangential CZ law' under mixed-mode conditions [49].

Following the above-mentioned approach, the distributions of interfacial shear stress in the coupled mixed-mode analysis can be simplified as a mode-II analysis with replacing the bond-slip relationship as the "effective tangential CZ law". Thus, the governing equations and boundary conditions in *E-S* stage in single mode-II analysis are still hold for the coupled mixed-mode analysis. And the relationship between the length of the softening region ($\bar{x}$) and the applied mechanical and thermal loading (F and ΔT) is still applicable in the coupled mixed-mode analysis, but with different input parameters (i.e., from 'τ_p' to $\tau_{p,eff}$, from 'K_T'' to '$K_{T,eff}'$'). As a consequence, the length of the softening zone ($\bar{x}$) can be calculated by the following function (refer to Eq.3):

$$F = 2\{\tau_{p,eff}\{\tan(\lambda'_{eff}\bar{x}) + r_{eff}\coth[\lambda(l-\bar{x})]\} + \frac{m'_{3,eff}\Delta T}{\lambda'_{eff}\cos(\lambda'_{eff}\bar{x})}\} / \{\frac{m_1\sin(\lambda'_{eff}\bar{x}) + \frac{m'_{2,eff}a}{\lambda'_{eff}}}{\cos(\lambda'_{eff}\bar{x})} + m_1 r_{eff}\frac{\cosh[\lambda(l-\bar{x})]-1}{\sinh[\lambda(l-\bar{x})]}\} \tag{56}$$

where,

$${\lambda'_{eff}}^2 = \frac{K'_{T,eff}}{K_T}\lambda^2,\ m'_{2,eff} = \frac{K'_{T,eff}y_1}{E_1 I_1},\ r_{eff} = \frac{\lambda'_{eff}}{\lambda} = \sqrt{\frac{K'_{T,eff}}{K_T}},\ m'_{3,eff} = K'_{T,eff}(\alpha_2 - \alpha_1)$$

Then the problem turns into the determination of the parameters in the 'effective tangential CZ law', including $\tau_{p,eff}$ and $K'_{T,eff}$.

In *E-S* stage, the maximum interfacial shear stress ($\tau_{p,eff}$) is located at the connection point between the softening and elastic region (i.e., $x = \bar{x}$) and can be calculated by multiplying the interfacial slip [i.e., $\delta_t^{es}(\bar{x})$] with the interfacial shear stiffness (K_T):

$$\tau_{p,eff} = K_T\delta_t^{es}(\bar{x}) \le \tau_p \tag{57}$$

In addition, the stiffness in the softening branch ($K'_{T,eff}$) can be calculated as the slope between the two points in **Fig. 6b**, including $[\delta_t^{es}(\bar{x}), \tau_{p,eff}]$ and $\{\delta_t^{es}(0), [1 - d(0)]K_T\delta_t^{es}(0)\}$.

$$K'_{T,eff} = K_T\frac{\delta_t^{es}(\bar{x}) - [1-d(0)]\delta_t^{es}(0)}{\delta_t^{es}(0) - \delta_t^{es}(\bar{x})} = K_T\frac{1-[1-d(0)]\frac{\delta_t^{es}(0)}{\delta_t^{es}(\bar{x})}}{\frac{\delta_t^{es}(0)}{\delta_t^{es}(\bar{x})} - 1} \tag{58}$$

According to Eqs. (57) and (58), $\tau_{p,eff}$ and $K'_{T,eff}$ depend on the damage variable at plate end $[d(0)]$, the interfacial slip at both the plate end $[\delta_t^{es}(0)]$ and the connection point between the elastic and softening region $[\delta_t^{es}(\bar{x})]$, and the length of softening zone ($\bar{x}$).

In *E-S* stage, $d(0)$ can be calculated by substituting the interfacial slip at plate end $[\delta_m^{es}(0)]$ into Eq. (16),

$$d(0) = \frac{\delta_m^f[\delta_m^{es}(0) - \delta_m^0]}{\delta_m^{es}(0)(\delta_m^f - \delta_m^0)} \tag{59}$$

In which, the mixed-mode deformation at onset of softening and debonding (i.e., δ_m^0 and δ_m^f) can be calculated by substituting the mode-mixity ratio in *E-S* stage at plate end and the junction point [i.e., $\gamma^{es}(0)$ and $\gamma^{es}(\bar{x})$] into Eqs. (9) and (13) as follows,

$$\delta_m^0 = \begin{cases} \delta_t^0 \delta_n^0 \sqrt{\frac{1+\gamma^{es}(\bar{x})^2}{\delta_t^{0\,2} + \gamma^{es}(\bar{x})^2}} & if\ \delta_n^0 > 0 \\ \delta_t^0 & if\ \delta_n^0 \leq 0 \end{cases} \tag{60}$$

$$\delta_m^f = \frac{2[1+\gamma^{es}(0)^2]}{\delta_m^0}\left[\left(\frac{K_N}{G_{IC}}\right)^\alpha + \left(\frac{\gamma^{es}(0)^2 K_T}{G_{IIC}}\right)^\alpha\right]^{-1/\alpha} \tag{61}$$

According to the equations from (57) to (61), the dominant parameters in 'effective tangential CZ law', including $\tau_{p,eff}$ and $K'_{T,eff}$, can be solved provided that the magnitudes of interfacial slip and damage variable at plate end and the connection point [i.e., $\delta_t^{es}(0)$, $\delta_t^{es}(\bar{x})$, $\gamma^{es}(0)$, $\gamma^{es}(\bar{x})$] are known. The subsequent sections focus on the derivation process of these unknown parameters. De Lorenzis et al.'s model [49] adopted two assumptions for simplifying the derivation process of the above-mentioned four parameters for the mixed-mode analysis under mechanical loading only: (1) the normalized Mode-II slip/Mode I seperation distributions along the inteface at different load levels are constant. Dai et al. [53] also proved theoretically that the normalized strain distriubtions of FRP (i.e., by the maximum FRP strain value) along an FRP-to-concrete interface are unique under different load levels if the bond-stress slip relationship at different location is constant. (2) a constant mode-mixity at the plate-end for *E* stage and *E-S* stages. To investigate if the above two assumptions are applicable for the mixed-mode analysis under combined mechanical loading and temperature variation, the FE analyses are conducted. The previous experimentally studied beam (i.e., specimen S304) by Deng and Lee [2] is taken as an example. The FE results will be first presented, while the detailed information about the FE model will be presented in the later sections.

Constant normalized interfacial shear slip/separation assumption

Fig. 7 compares the distributions of interfacial shear slip/separation under single mechanical loading (i.e., 80 kN, 0°C; 120 kN, 0°C) and combined mechanical loading and temperature variation (i.e., 60 kN, 40°C; 110 kN, 40°C) over the bond length obtained from the FE modeling. Both E and E-S stage are included in these figures. The magnitudes of interfacial shear slip/separation along the bondline are normalized by their magnitudes at the plate end [i.e., $\delta_t^e(0)$ and $\delta_n^{es}(0)$]. It is clear that all the normalized distributions converge to a single curve. In other words, the normalized interfacial slip/separation in both *E* stage and *E-S* stage are identical regardless of the load level and the magnitude of temperature variation. And the absolute magnitudes of interfacial slip/separation along the bondline in *E-S* stage can be obtained by multiplying the interfacial slip/separation in *E* stage [i.e., Eq. (52) and Eq. (53)] with a coefficient φ_T, and φ_N, respectively.

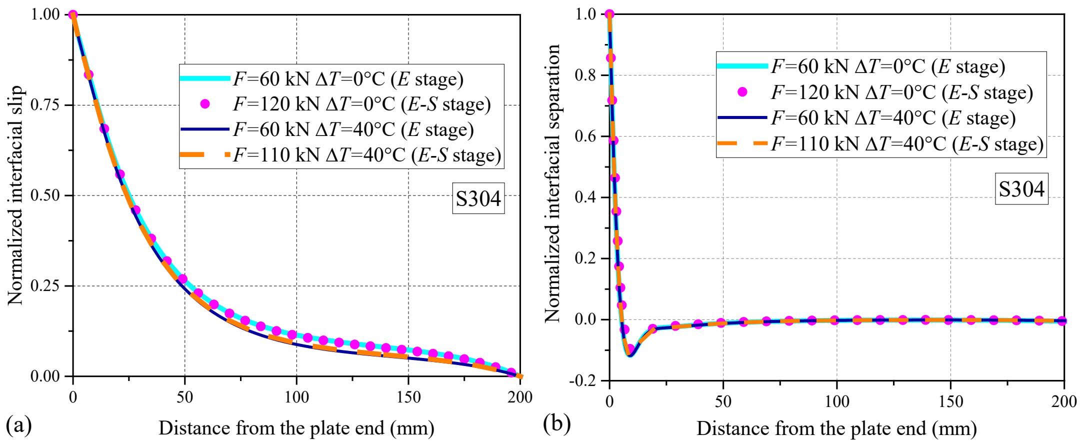

Fig. 7 Distribution of normalized a) interfacial slip [$\delta_t^{es}(x)/\delta_t^{es}(0)$] and b) separation [$\delta_n^{es}(x)/\delta_n^{es}(0)$] under various loadings.

Thus, the distributions of interfacial slip and separation in *E-S* stage can be expressed as follows,

$$\delta_t^{es}(x) = \frac{\varphi_T}{K_T}[B_1 \cosh(\lambda x) + B_2 \sinh(\lambda x) + m_1 \frac{F}{2}];\ 0 < x < l \qquad (62)$$

$$\delta_n^{es}(x) = \frac{\varphi_N}{K_N}\{e^{-\beta x}[C_1\cos(\beta x) + C_2\sin(\beta x)] - n_1\lambda[B_1\sinh(\lambda x) + B_2\cosh(\lambda x)]\}; 0 < x < l \tag{63}$$

where φ_T and φ_N are the amplification factors.

By substituting $x = 0$ into the above equation, the magnitudes of interfacial slip and separation at plate end can be expressed as

$$\delta_t^{es}(0) = \frac{\varphi_T}{K_T}\left(B_1 + m_1\frac{F}{2}\right) \quad \delta_n^{es}(0) = \frac{\varphi_N}{K_N}(C_1 - n_1\lambda B_2) \tag{64}$$

In addition, the interfacial stresses at the conjunction point between elastic and softening regions ($x = \bar{x}$) should satisfy the quadratic stress failure criterion [Eq. (7)] as follows:

$$\{\frac{\varphi_T}{\tau_p}\left[B_1\cosh(\lambda\bar{x}) + B_2\sinh(\lambda\bar{x}) + m_1\frac{F}{2}\right]\}^2 + \{\frac{\varphi_N}{\sigma_p}\langle e^{-\beta x}[C_1\cos(\beta\bar{x}) + C_2\sin(\beta\bar{x})] - n_1\lambda[B_1\sinh(\lambda\bar{x}) + B_2\cosh(\lambda\bar{x})]\rangle\}^2 = 1 \tag{65}$$

And for a given $\bar{x}$, the amplification factors can be solved as,

$$\frac{1}{{\varphi_T}^2} = \frac{1}{{\varphi_N}^2} = \left[\frac{1}{\tau_p}\left(B_1\cosh(\lambda\bar{x}) + B_2\sinh(\lambda\bar{x}) + m_1\frac{F}{2}\right)\right]^2 + \{\frac{1}{\sigma_p}\langle \mathrm{e}^{-\beta x}[C_1\cos(\beta\bar{x}) + C_2\sin(\beta\bar{x})] - n_1\lambda[B_1\sinh(\lambda\bar{x}) + B_2\cosh(\lambda\bar{x})]\rangle\}^2 \tag{66}$$

Here, $\varphi_N = \varphi_T$ is assumed and the reason will be discussed in next section.

Mode-mixity ratio assumption

Fig. 8 shows the variation of mode-mixity ratio (γ) at two different locations (i.e., x = 0 mm and 4 mm) under increasing levels of mechanical loading in the FE results. It is clear that the mode-mixity ratio reduces significantly at locations away from the plate end (e.g., x=4 mm) during the *E-S* stage. However, at the plate end location (i.e., x = 0), the reduction of the mode-mixity ratio is marginal from the *E* stage to *E-S* stage and only becomes very significant after the interface enters into debonding stage. The temperature variation changes the load when the interface starts entering into the *E-S* stage (i.e., onset of the softening in **Fig. 8**), but does not change the above-mentioned trend.

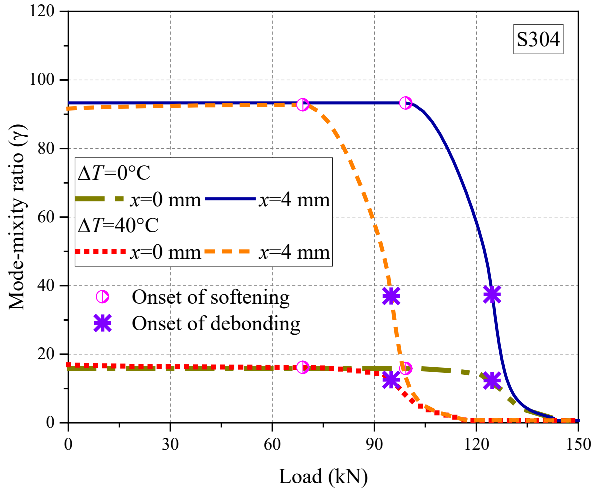

Fig. 8 Variation of mode-mixity ratio (γ) at different locations under increasing mechanical loading.

To further investigate how the mode-mixity ratio (γ) changes at different locations during the interfacial debonding failure process, **Fig. 9** compares the mode-mixity ratio (γ) at different locations at the *E* stage and end of the *E-S* stage (i.e., γ^{deb} at the debonding load). Again, it is shown that the mode-mixity change is independent of temperature variation at any location. However, the mode-mixity ratios during both *E* stage (represent by γ^{e} at the end of *E* stage) and *E-S* stage (represent by γ^{deb} at the end of *E-S* stage) increase with the distance from the plate end. At the plate end, the difference between $\gamma^{e}$and $\gamma^{deb}$is the minimum while at a distance the γ^{deb}value is usually smaller than the γ^{e} value, indicating that the mode-mixity ratio reduces when the bond interface shifts from *E* stage to *E-S* stage. while the reduction seems to be more significant when the location is further away from the plate end.

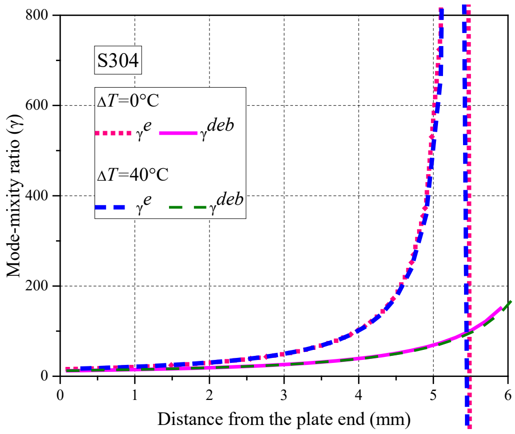

Fig. 9 Distributions of mode-mixity ratio (γ) at different locations near the plate end.

Following De Lorensis et al. [49], here it is also assumed that the magnitude of mode-mixity ratio in *E-S* stage is equal to that in *E* stage at the plate end and [i.e., $\gamma^{es}(0) = \gamma^{e}(0)$].

Accordingly, the mode-mixity ratio at the plate end in *E-S* stage can be calculated as

$$\gamma^{es}(0) = \frac{\delta_t^{es}(0)}{\delta_n^{es}(0)} = \frac{\varphi_T}{\varphi_N}\frac{\delta_t^{e}(0)}{\delta_n^{e}(0)} \tag{67}$$

In *E* stage, $\gamma^{e}(0) = \frac{\delta_t^{e}(0)}{\delta_n^{e}(0)}$. Therefore, $\varphi_T = \varphi_N$.

Apart from the magnitude of γ^{es} at the plate end (i.e., $x = 0$ mm), the magnitude of γ^{es} at the connection point between elastic and softening region ($x = \bar{x}$) should be paid special attention, because it determines the key parameters of the softening branch in the 'effective tangential CZ law' (i.e., $\tau_{p,eff}$ and $K'_{T,eff}$).

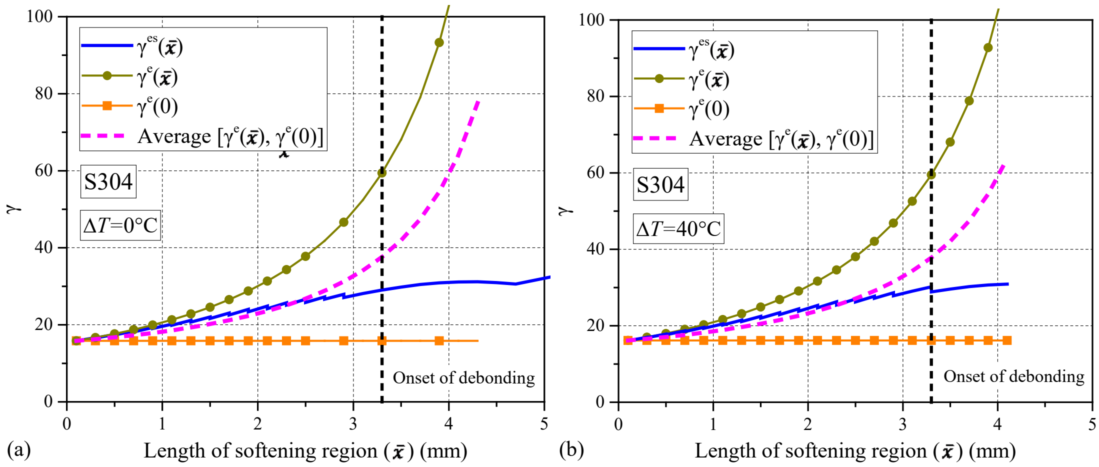

Fig. 10 Variation of mode-mixity ratio (γ) with $\bar{x}$: a) $\Delta T = 0$°C; b) $\Delta T = 40$°C.

When the interface changes from E stage to E-S stage, there is a location $\bar{x}$, representing the connection point of elastic and softening regions. **Fig. 10** presents the mode-mixity ratios of the location $\bar{x}$ at the ends of E-stage (i.e., $\gamma^{e}(\bar{x})$ in **Fig. 10**) and E-S stage (i.e., $\gamma^{es}(\bar{x})$ in **Fig. 10**), respectively. **Fig. 10a** and **Fig. 10b** represent FRP-strengthened steel beams under mechanical loading and combined themal and mechanical loading, respectively. The mode-mixity ratio at the plate end ($\gamma^{e}(0)$) is also provided in the figure as a reference. The vertical line indicates that the interface starts debonding when $\bar{x}$ reaches that value. In De Lorenzis et al.'s model [49], it was assumed $\gamma^{es}(\bar{x}) = \gamma^{es}(0) = \gamma^{e}(0)$ for FRP-strengthened steel beam at mechanical loading in the E-S stage. It seems such approximation is a bit rough considering the obvious difference between $\gamma^{es}(\bar{x})$ and $\gamma^{e}(0)$ (see **Fig. 10a**). Instead, it is more rational to approximate $\gamma^{es}(\bar{x})$ as the average of $\gamma^{e}(0)$ and $\gamma^{e}(\bar{x})$ (see the pink dotted lines in both **Fig. 10a** and **Fig. 10b**), since it is difficult to obtain the explicit solution for $\gamma^{es}(\bar{x})$. Accordingly,

$$\gamma^{es}(\bar{x}) = \frac{\gamma^{e}(0) + \gamma^{e}(\bar{x})}{2} \tag{68}$$

In E-S stage, for deriving the interfacial behavior of FRP-strengthened steel beam, $\bar{x}$ should be calculated in advance based on the given parameters, the applied loading, and the boundary condition, since the bond-slip equations are different at the two sides of $\bar{x}$. When adopting the 'effective tangential CZ law', both the $\tau_{p,eff}$ and $K_{T,eff}^{'}$ are also dependent on the magnitude of $\bar{x}$, which is unknown before the calculation. In this paper, an iteration process (realized through Matlab) is deployed to solve this problem as explained in the next section.

Analytical Flowchart for Obtaining the Interfacial Behavior in E-S Stage

Fig. 11 presents the calculation procedure of the interfacial stresses of FRP-strengthened steel beam. When the interface is in the E stage, the distributions of interfacial stresses can be determined by Eqs. (33) and (45). Once the interface enters the E-S stage, the interfacial behavior can be determined iteratively as follows:

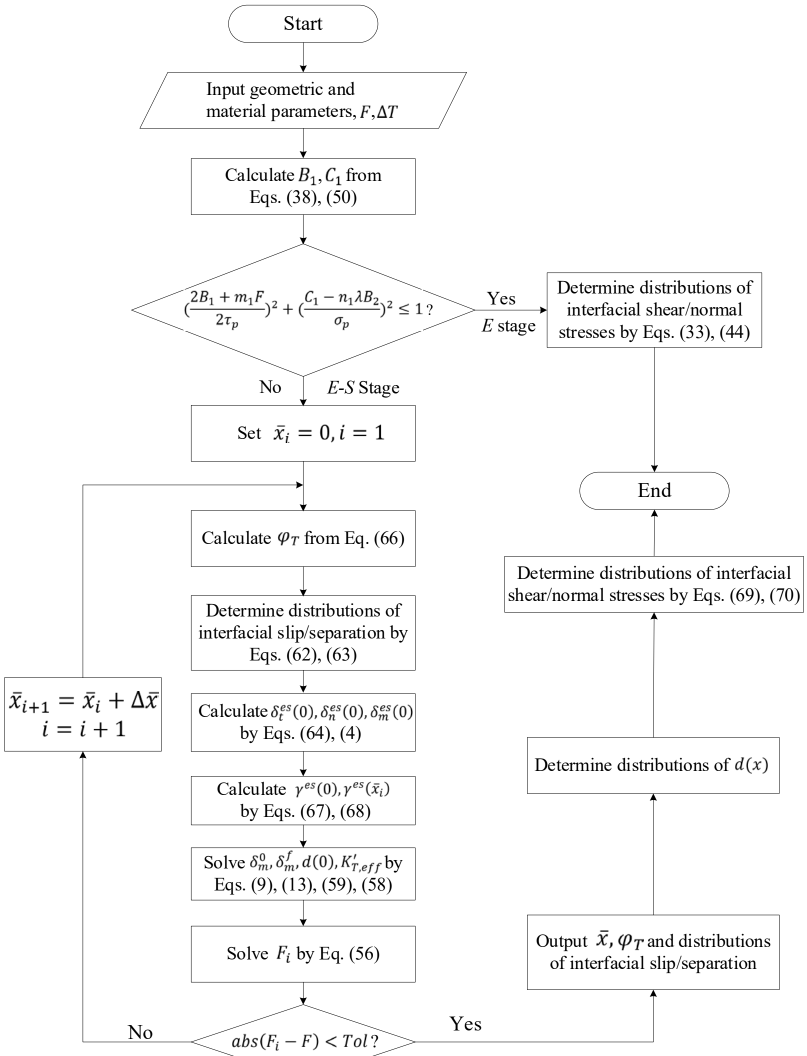

Fig. 11 Analytical flow chart for obtaining the interfacial behavior in E-S stage.

1. Set $\bar{x}_i = 0$, the corresponding value of magnification factor (φ_T) can be calculated by Eq. (66). Based on which, the distributions of interfacial slip/separation can be obtained by Eq. (62) and Eq. (63). Then, the magnitude of $\delta_t^{es}(\bar{x}_i)$ and $\tau_{p,eff}$ can be calculated by Eq. (62) and Eq. (57), respectively. In addition, the magnitudes of $\delta_t^{es}(0)$ and $\delta_n^{es}(0)$ at plate end can be calculated by Eq. (64), then $\delta_m^{es}(0)$ can be calculated by Eq. (4).

2. Then the mode-mixity ratio at plate end, $\gamma^{es}(0)$, and the assumed location, $\gamma^{es}(\bar{x}_i)$, can be calculated by Eqs. (67) and (68). Once $\gamma^{es}(0)$ and $\gamma^{es}(\bar{x}_i)$ are available, δ_m^0 and δ_m^f can be calculated through Eq. (9) and Eq. (13), respectively. Based on δ_m^0, δ_m^f and $\delta_m^{es}(0)$, $d(0)$ can be calculated by Eq. (59).

3. When $d(0)$ is determined, the slope of effective softening branch ($K'_{T,eff}$) can be calculated by Eq. (58). Then the parameters in 'effective tangential CZ law', including the slope of elastic branch (K_T), peak shear strength ($\tau_{p,eff}$) and the slope of softening branch ($K'_{T,eff}$) are given at $\bar{x}_i$.
4. The magnitude of F_i corresponding to the trial $\bar{x}_i$ can be calculated by Eq. (56). Initially, F_i is smaller than the applied load. Then, the magnitude of $\bar{x}_i$ is slightly increased and Step 1~3 is repeated until the convergence is reached. Substituting the determined $\bar{x}$, φ_T into the Eqs. (62) and (63), the distributions of interfacial slip/separation in *E-S* stage [i.e., $\delta_t^{es}(x)$ and $\delta_n^{es}(x)$] can be derived.
5. At last, the distribution of $d(x)$ in Eq. (70) can be derived through Eq. (16), to which the $\delta_t^{es}(x)$ and $\delta_n^{es}(x)$ are substituted. Then, based on the obtained interfacial slip/separation [$\delta_t^{es}(x)$ and $\delta_n^{es}(x)$] and damage variable [$d(x)$], the distributions of interfacial bond/normal stresses in *E* stage and *E-S* stage can be obtained as follows:

$$\tau^{es}(x) = K_T\delta_t^{es}(x);\ \sigma^{es}(x) = K_N\delta_n^{es}(x)\ (\bar{x} < x < l) \tag{69}$$

$$\tau^{es}(x) = [1 - d(x)]K_T\delta_t^{es}(x);\ \sigma^{es}(x) = [1 - d(x)]K_N\delta_n^{es}(x)\ (0 < x < \bar{x}) \tag{70}$$

Prediction of the Debonding Load

The debonding load is achieved at end of the *E-S* stage, when $\delta_m^{es}(0) = \delta_m^f$ and $\tau^{es}(0) = 0$. Therefore, at a given ΔT, set $F = F_{sof}$ and gradually increase the magnitude of F. For each trial value of F, check the magnitude of shear stress at plate end [$\tau^{es}(0)$] that resultant from the iteration calculation in the previous section. $\tau^{es}(0)$ decreases as the increase of trial magnitude of F, and the debonding load is achieved when $\tau^{es}(0)$ decreases to zero.

Results and Discussion

Validation of the Analytical Solution

The FE modeling are conducted by using the general-purpose software ABAQUS [54], which has been used in the authors' research group for modeling the behavior of FRP-strengthened reinforced concrete (RC) beams at ambient temperature and under fire exposure [55-58], the debonding behavior of FRP-to-steel/concrete bonded joints under combined thermal and mechanical loading [17, 18], and the debonding failures of the FRP-strengthened steel beams [6, 40, 41, 47].

In the FE model, both the steel beam and FRP plate are modeled by 2-node cubic beam element (B23), and the adhesive layer is modeled by 4-node two-dimensional cohesive element (COH2D4). As shown in **Fig. 12**, the steel beam and FRP plate are tied by cohesive element at the reference line of both adherends and the adhesive layer, rather than their centroidal axes [59].

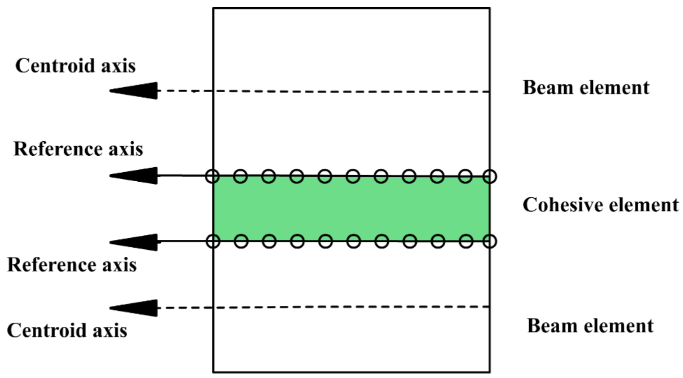

Fig. 12 Schematic of the element types and reference axes of the beam and FRP plate.

According to the mesh convergence study by Guo et al. [41], the length of the beam element is taken as 0.2 mm for both steel beam and FRP plate. The size of the elements at the adhesive layer is 0.2*1 mm (with 1 mm in thickness).

The beams S303 and S304 (i.e., steel beam under three-point bending and strengthened by 0.3 m or 0.4 m FRP plate) presented in Deng et al.'s experimental study [2] were selected as the studied case in this paper. The layout and the loading condition of the strengthened beam are shown in **Fig. 1**. And the mechanical parameters of both adherends and the interface are summarized in **Table 1**.

Table 1 Parameters used in the FE model.

Geometry data				S304	S303
y_1 (mm)	A_1 (mm^2)	I_1 (mm^4)	b_2 (mm)	l (mm)	l (mm)
63.5	1602	4.59*10^6	76	200	150
y_2 (mm)	A_2 (mm^2)	I_2 (mm^4)	t_a (mm)	a (mm)	a (mm)
1.5	228	171	1.0	350	400

Material and interface bond behavior data					
E_1 (N/mm^2)	α_1 (/°C)	τ_p (N/mm^2)	δ_t^0 (mm)	δ_t^f (mm)	G_{II} (N/mm)
205000	11*10^{-6}	26.7	0.0526	0.1191	1.59
E_2 (N/mm^2)	α_2 (/°C)	σ_p (N/mm^2)	δ_n^0 (mm)	δ_n^f (mm)	G_I (N/mm)
212000	6*10^{-7}	29.7	0.00371	0.004	0.0594

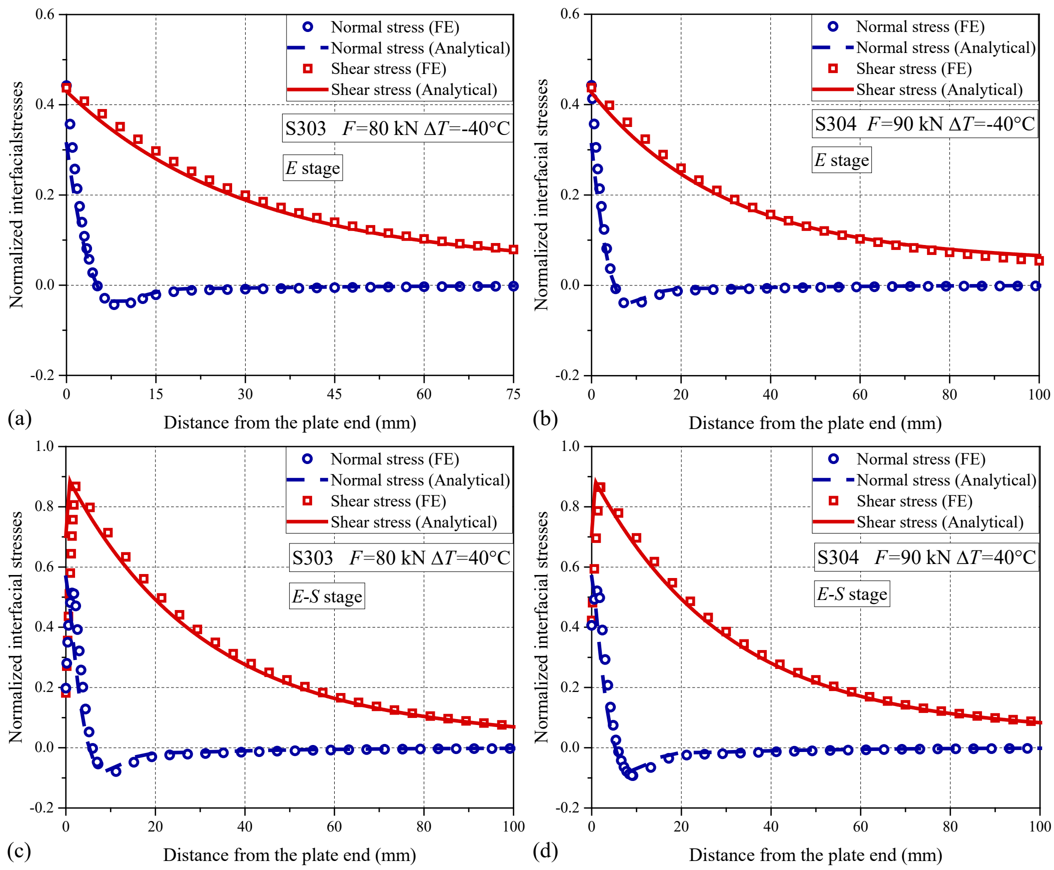

Fig. 13 Comparison of interfacial stresses from FE and analytical solution: a) S303 at 80 kN and -40°C; b) S304 at 90 kN and -40°C; c) S303 at 80 kN and 40°C; d) S304 at 90 kN and -40°C.

Fig. 13 compares the distributions of interfacial shear and normal stresses with the magnitude normalized by τ_p and σ_p, respectively. The dotted lines represent analytical results, while the continuous lines represent FE modeling results. To clearly show the interfacial behavior near the plate end, only a quarter length of FRP plate starting from the plate end is shown in **Fig. 13**. Both the mechanical loading (i.e., 80 kN for S303; 90 kN for S304) and temperature variation (i.e., -40°C and 40°C) are considered. It can be observed that the distributions of interfacial shear/normal stresses from the analytical solutions are in good agreement with the FE results. Therefore, the validity of the proposed analytical approach for predicting the interfacial bond behavior of FRP-strengthened beam under combined mechanical and thermal loading is confirmed.

As shown in **Fig. 13**, the deformation stages of two beams are *E* stage at -40°C and *E-S* stage at 40°C respectively, although the load level is the same. This phenomenon is resulted from the interfacial thermal stress as discussed below.

In the ΔT = -40°C case (**Fig. 13a, b**), the maximum shear stresses can be observed at the plate end, and the magnitude of shear stress decreases with the distance to the plate end. The direction of the interfacial shear stress remains unchanged from the plate end to the middle span of the FRP plate. In comparison, the interfacial normal stress is tensile (positive value) at the plate end while turns to compressive (negative value) at locations away from the plate end. Besides, the magnitudes of both shear and normal interfacial stresses decrease to zero at the middle length of FRP plate. While at ΔT = 40°C (**Fig. 13c, d**), the interface is in *E-S* stage, with the softening region occurs near the plate end. In comparison to the distribution of interfacial stress derived by mode-II analysis only (**Fig. 3**), the peak interfacial stress in the mix-mode analysis is less than τ_p.

Comparison with Previous Results

Table 2 The loads at the onset of softening and debonding at normal temperature.

At normal temperature (ΔT=0)	Debonding load (kN)				Softening onset load (kN)	
	Experimental results [2]	FE results [47]	Analytical solution [49]	Proposed analytical solution	FE results [47]	Proposed analytical solution
S303	120	118	138	127	84	98
S304	135	132	155	142	117	111

Table 2 compares the load at onset of softening and debonding at normal temperatures obtained from the analytical solutions proposed in this paper, the coupled mixed-mode analysis proposed by De Lorenzis et al. [49], and FE modeling [47] with the experimental results [2]. It can be observed that both the FE modeling and analytical solutions provide closer predictions of the experimental results. Specifically, the FE results give almost the identical predictions with the experimental data, because of the consideration of the geometric imperfection and nonlinear constitutive law of the steel beam [47]. In comparison, a slightly larger difference can be observed between the experimental data and analytical results, which could be attributed to the simplified assumptions on the mode-mixty ratio at $\bar{x}$ in E-S stage [i.e., $\gamma^{es}(\bar{x})$] as mentioned above. In addition, in experiments, the steel beam already exhibited some yielding at the ultimate failure.

Table 3 The loads at the onset of softening at changed temperatures.

Softening onset load (kN)	Temperature variation (ΔT)	-40°C	-20°C	0°C	20°C	40°C
S303	Single mode-II analysis [41]	148	134	120	105	91
	Proposed analytical solution	126	112	98	84	70
S304	Single mode-II analysis [41]	168	151	135	119	103
	Proposed analytical solution	142	127	111	95	79

Table 4 The loads at the onset of debonding at changed temperatures.

Debonding load (kN)	Temperature variation (ΔT)	-40°C	-20°C	0°C	20°C	40°C
S303	Single mode-II analysis [41]	201	187	174	160	146
	Proposed analytical solution	154	140	127	113	99
S304	Single mode-II analysis [41]	226	210	195	180	164
	Proposed analytical solution	174	159	142	127	112

Table 3 and **Table 4** compare the predicted mechanical loading at the onset of softening and debonding that predicted by the single mode-II [41] and proposed coupled mixed-mode analyses. Despite the same bond-slip relationship in mode-II directions being adopted in both analytical solutions, the single mode-II analysis tends to overestimate the debonding load at all temperature levels, because of the neglection of the interfacial normal stress effect. For both S303 and S304 under mechanical loading, the debonding load is increased by about 45% from the onset of softening till the debonding in mode-II analysis, while such increase is 29% only in the mixed-mode analysis. The length of softening region at debonding load is around 32.0 mm in mode-II analysis but 3.9 mm only in coupled mixed-mode analysis. These phenomena can be resultant from the decreased fracture energy in the softening stage, as described the 'effective tangential CZ law'.

In addition, the mechanical loading at the onset of softening and debonding of FRP-strengthened steel beam are dramatically affected by the temperature variation. For beams S303 and S304, the increase of service temperature from -40°C to 40°C (which could happen by seasonal temperature change) leads to a decrease of about 35% of the debonding load, and thus would lead to the premature failure of the structure. Therefore, an in-depth understanding of the thermal effect on the debonding behavior of the FRP-strengthened steel beam is essential for the safe strengthening design.

Interfacial Stress Distribution under Combined Mechanical and Thermal Loading

Fig. 14 shows the distributions of interfacial stresses in both shear and normal directions of the FRP-strengthened steel beam S304 under combined mechanical (110 kN) and thermal loading (ΔT ranges from -40°C to 40°C). It can be observed that the interface evolves from *E* stage to *E*-*S* stage as the temperature increases.

When $\Delta T \leq 0$°C, the entire bond length is in the elastic stage and the magnitude of the interfacial stresses at each point increase with ΔT. After the softening criterion (Eq. 17) is satisfied, the softening occurs at the plate end and the shear stress in the softening region decreases subsequently as the temperature increase. It can be expected that the plate-end debonding could happen with the further increase of temperature.

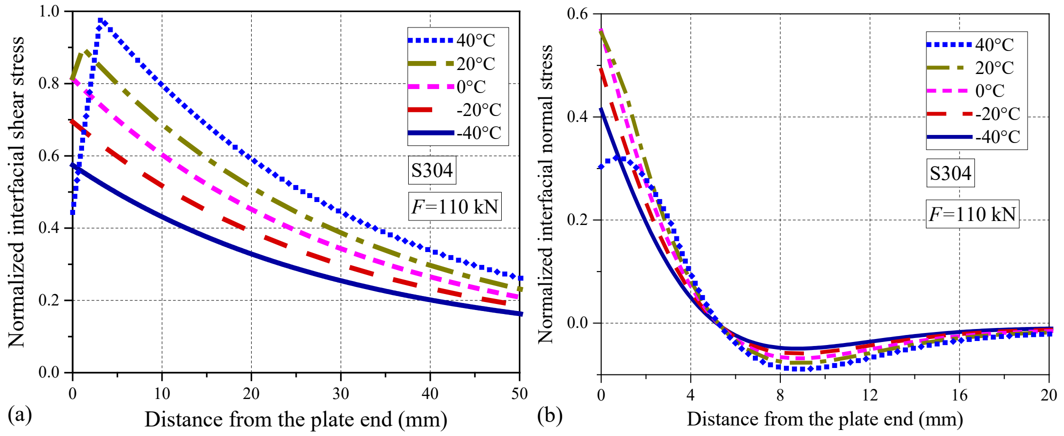

Fig. 14 Interfacial stress distributions of FRP-strengthened steel beam under combined mechanical and thermal loading: a) normalized interfacial shear stress; b) normalized interfacial normal stress.

To better explain this phenomenon, the interfacial behavior under mechanical or thermal loading is separately investigated in **Fig. 15** and **Fig. 16**.

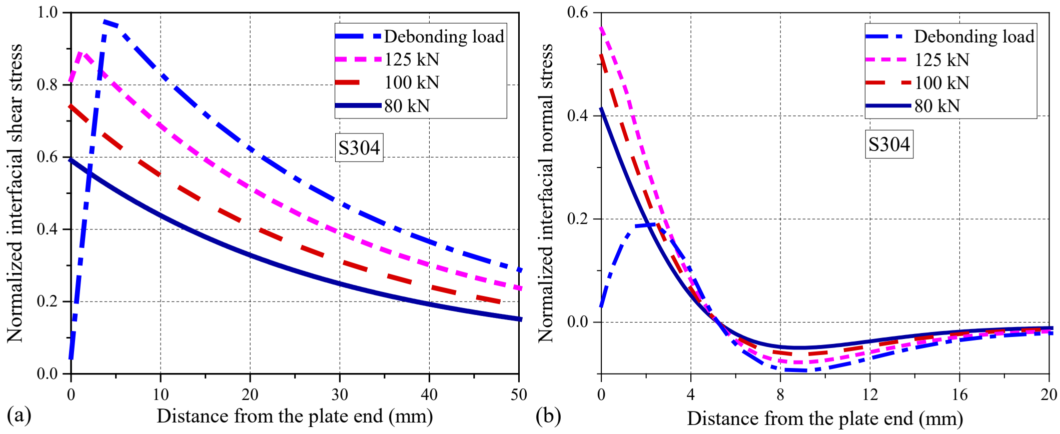

Fig. 15 Interfacial stress distributions of FRP-strengthened steel beam under various mechanical loading: a) normalized interfacial shear stress; b) normalized interfacial normal stress.

Fig. 15 presents the distributions of interfacial shear and normal stresses in beam S304 under increasing mechanical loading. As the load increases, the bonding interface evolves from *E* stage (80 kN and 100 kN) to *E-S* stage (125 kN) and the trend is similar to that under constant loading and increasing temperature (**Fig. 14**). In addition, despite the different deformation stages experienced by the interface, the magnitude of interfacial stress in both directions are all positive near the plate end.

Fig. 16 shows the distributions of interfacial stresses under single thermal loading. When a temperature decrease is applied to the FRP-strengthened steel beam, negative interfacial stresses are generated at the bond interface (**Fig. 16**) near plate end. And the directions of interfacial stresses in shear and normal directions are opposite to those generated by the mechanical loading (**Fig. 15**). The interfacial stresses from both mechanical and thermal loading can be superimposed on each other. As such, the magnitudes of interfacial stresses that caused by the mechanical loading (**Fig. 15**) are reduced near the plate end. Because of the lower interfacial stresses at -40°C and -20°C as comparing to the 0°C case under same mechanical loading, a higher level of mechanical load is needed at onset of softening and debonding.

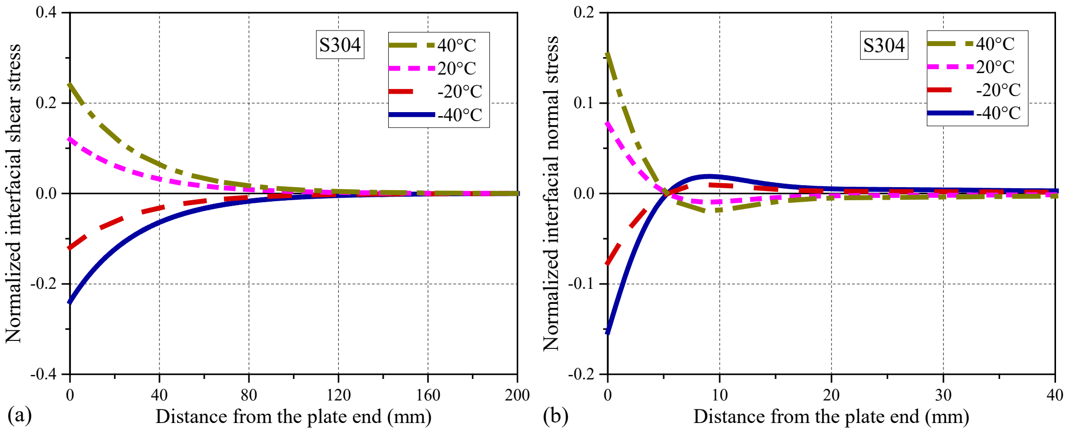

Fig. 16 Interfacial stress distributions of FRP-strengthened steel beam under single thermal loading: a) normalized interfacial shear stress; b) normalized interfacial normal stress.

On the contrary, the interfacial stresses caused by a temperature elevation (**Fig. 16**) are in the same direction as that caused by the mechanical loading (**Fig. 15**). Thus, a higher level of damage of interface can be achieved at elevated temperature given the same mechanical loading (**Fig. 14**). As a consequence, the required mechanical loading at onset of softening and debonding should be lower. In summary, the onset of softening and debonding is delayed at decreased temperatures while accelerated at increased temperatures.

Parametric Study

To investigate the effect of the bond and FRP properties on the plate-end debonding load under temperature variations, a parametric study was further conducted using the proposed analytical approach.

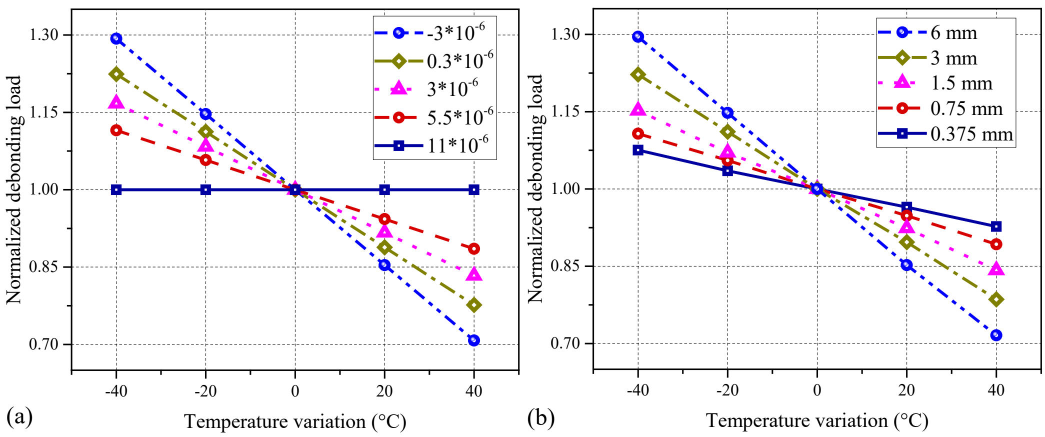

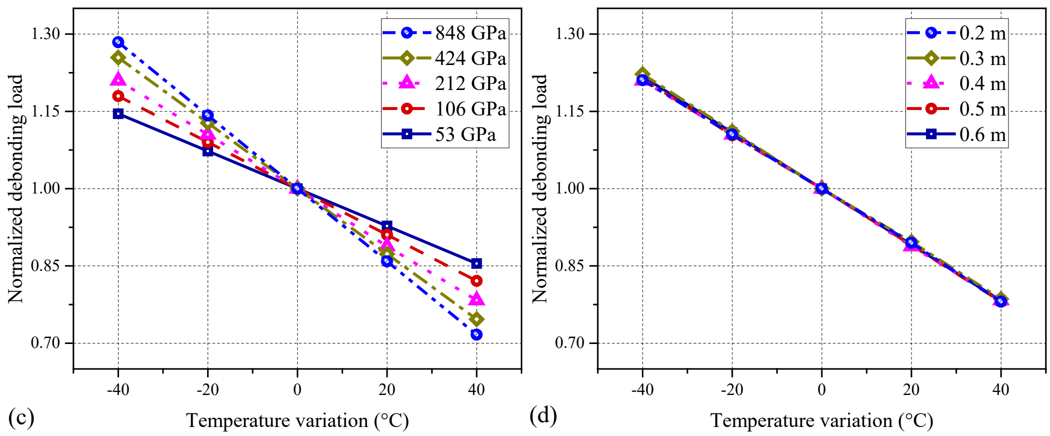

Fig. 17 Effect of temperature variation on normalized debonding load of the FRP-strengthened steel beam at different plate: a) CTEs; b) thicknesses; c) elastic moduli; d) lengths.

Fig. 17 presents the changes of plate-end debonding load with the temperature variation of the same steel beam strengthened by different FRP plates, in terms of plate thickness (**Fig. 17a**), length (**Fig. 17b**), elastic moduli (**Fig. 17c**) and CTE (**Fig. 17d**). In this figure, the plate-end debonding load at various temperatures is normalized by the value at ambient temperature (i.e., ΔT = 0°C).

According to **Fig. 17a**, when the CTEs of FRP plate and steel beam are identical (i.e., $1.1*10^{-6}$), the predicted debonding loads are the same at different temperatures because of the nonexistence of thermal stress effect. For the FRP plate with a CTE lower than steel, the debonding load decreases linearly with the temperature increase, regardless of the FRP thickness and length. The thermal stress effect becomes more significant when the difference in CTE between FRP and steel is higher.

According to **Fig. 17b** and **Fig. 17c**, the steel beams strengthened with thicker and stiffer FRP plates are more sensitive to the temperature elevation. For an extreme case, when an 80°C (i.e., from -40°C to 40°C) temperature increase was applied, 60% decrease of the debonding load can be observed for the steel beam strengthened with a 6 mm and 212 GPa FRP plate. In comparison, the effect of the FRP length on the change of debonding load is negligible (**Fig. 17d**). However, in view of that a shorter bond length usually leads to a lower debonding load, longer and thinner FRP plates are preferred to minimize the negative thermal stress effect on the safety of FRP-strengthened steel beams. If the use of a thicker or stiffer FRP plate is not avoidable, additional mechanical anchorages are needed to suppress the debonding failure.

Conclusions

This paper presents a closed-form analytical solution based on coupled mixed-mode cohesive zone model to analyze the interfacial behavior of FRP-strengthened steel beam under combined mechanical loading and thermal loading. The interfacial stresses in both tangential and normal directions are considered in predicting the loads at onset of softening and debonding of the FRP-to-steel interface. Based on the results of this study, several conclusions can be drawn as follows:

1. The proposed coupled mixed-mode analysis can provide an accurate prediction of the interfacial behavior and debonding load of FRP-strengthened steel beams under combined mechanical and thermal loading;
2. The interfacial behavior between the steel beam and FRP plate can be seriously affected by the temperature variation. The interfacial stress at elevated temperatures is in same direction as that generated by mechanical loading and thus accelerates the deformation process of the interface.
3. The debonding load of FRP-strengthened steel beam is significantly decreased by the temperature elevation. As such, special attention should be paid to the design of FRP-strengthened beams when the service temperature increase is expected.
4. The thermal stress is more significant when a thicker and stiffer FRP plate is adopted in strengthening the steel beam, for which case use of longer FRP plate and additional anchorages are preferred to reduce the negative effect of temperature increase.

Acknowledgements

The authors are grateful for the financial support received from the Hong Kong Research Grants Council - Theme-based Research Scheme (Project code: T22-5-2/18-

R), the National Natural Science Foundation of China (NSFC) (Project No: 51478406), the Research Grants Council of the Hong Kong SAR (Project No: 15219919), the National Foreign Expert Project of China (Project No: DL2021175003L and G2021175026L), and for a Ph.D. studentship awarded to the first author by The Hong Kong Polytechnic University.

Reference

[1] Teng JG, Yu T, Fernando D. Strengthening of steel structures with fiber-reinforced polymer composites. J Constr Steel Res. 2012;78:131-43.

[2] Deng J, Lee MMK. Behaviour under static loading of metallic beams reinforced with a bonded CFRP plate. Compos Struct. 2007;78:232-42.

[3] Lenwari A, Thepchatri T, Albrecht P. Debonding strength of steel beams strengthened with CFRP plates. J Compos Constr. 2006;10:69-78.

[4] Rizkalla S, Dawood M, Schnerch D. Development of a carbon fiber reinforced polymer system for strengthening steel structures. Compos Part a-Appl S. 2008;39:388-97.

[5] Yu Y, Chiew SP, Lee CK. Bond failure of steel beams strengthened with FRP laminates - Part 2: Verification. Compos Part B-Eng. 2011;42:1122-34.

[6] Zeng JJ, Gao WY, Liu F. Interfacial behavior and debonding failures of full-scale CFRP-strengthened H-section steel beams. Compos Struct. 2018;201:540-52.

[7] Colombi P, Poggi C. An experimental, analytical and numerical study of the static behavior of steel beams reinforced by pultruded CFRP strips. Compos Part B-Eng. 2006;37:64-73.

[8] Linghoff D, Haghani R, Al-Emrani M. Carbon-fibre composites for strengthening steel structures. Thin Wall Struct. 2009;47:1048-58.

[9] Sallam HEM, Ahmad SSE, Badawy AAM, Mamdouh W. Evaluation of steel I-beams strengthened by various plating methods. Adv Struct Eng. 2006;9:535-44.

[10] Stratford TJ, Bisby LA. Effect of Warm Temperatures on Externally Bonded FRP Strengthening. J Compos Constr. 2012;16:235-44.

[11] Sahin MU, Dawood M. Experimental Investigation of Bond between High-Modulus CFRP and Steel at Moderately Elevated Temperatures. J Compos Constr. 2016;20:04016049.

[12] Teng R, Guo Y, Wang H, Zhao Z, Wang X. Experimental study of bending interface characteristics of CFRP-strengthened long-span steel main beams at different temperatures. Eng Struct. 2021;235.

[13] Yoshitake I, Tsuda H, Itose J, Hisabe N. Effect of discrepancy in thermal expansion coefficients of CFRP and steel under cold temperature. Constr Build Mater. 2014;59:17-24.

[14] Silva MAG, Biscaia H. Degradation of bond between FRP and RC beams. Compos Struct. 2008;85:164-74.

[15] Dai JG, Gao WY, Teng JG. Bond-Slip Model for FRP Laminates Externally Bonded to Concrete at Elevated Temperature. J Compos Constr. 2013;17:217-28.

[16] Zhou H, Fernando D, Torero JL, Torres JP, Maluk C, Emberley R. Bond Behavior of CFRP-to-Steel Bonded Joints at Mild Temperatures: Experimental Study. J Compos Constr. 2020;24:04020070.

[17] Gao WY, Teng JG, Dai JG. Effect of temperature variation on the full-range behavior of FRP-to-concrete bonded joints. J Compos Constr. 2012;16:671-83.

[18] Gao WY, Dai JG, Teng JG. Analysis of Mode II debonding behavior of fiber-reinforced polymer-to-substrate bonded joints subjected to combined thermal and mechanical loading. Eng Fract Mech. 2015;136:241-64.

[19] Korayem AH, Chen SJ, Zhang QH, Li CY, Zhao XL, Duan WH. Failure of CFRP-to-steel double strap joint bonded using carbon nanotubes modified epoxy adhesive at moderately elevated temperatures. Compos Part B-Eng. 2016;94:95-101.

[20] Ferrier E, Rabinovitch O, Michel L. Mechanical behavior of concrete–resin/adhesive–FRP structural assemblies under low and high temperatures. Constr Build Mater. 2016;127:1017-28.

[21] Zhou H, Urgel JM, Emberley R, Maluk C, Fernando D. Behaviour of the FRP-to-steel bonded joints under elevated temperature. The 6th AsiaPacific conference on FRP in structures (APFIS 2017). Singapore: International Institute for FRP in Construction; 2017. p. 149–53.

[22] Biscaia HC, Ribeiro P. A temperature-dependent bond-slip model for CFRP-to-steel joints. Compos Struct. 2019;217:186-205.

[23] Chandrathilaka E, Gamage J, Fawzia S. Mechanical characterization of CFRP/steel bond cured and tested at elevated temperature. Compos Struct. 2019;207:471-7.

[24] Nguyen PL, Vu XH, Ferrier E. Elevated temperature thermomechanical behaviour of near surface mounted CFRP reinforced concrete specimens: Effect of adhesive at concrete/CFRP interface. Eng Struct. 2019;197:109361.

[25] Ke L, Li C, He J, Dong S, Chen C, Jiao Y. Effects of elevated temperatures on mechanical behavior of epoxy adhesives and CFRP-steel hybrid joints. Compos Struct. 2020;235:111789.

[26] Zhou A, Qiu Q, Chow CL, Lau D. Interfacial performance of aramid, basalt and carbon fiber reinforced polymer bonded concrete exposed to high temperature. Compos Part a-Appl S. 2020;131:105802.

[27] Biscaia HC, Chastre C, Viegas A, Franco N. Numerical modelling of the effects of elevated service temperatures on the debonding process of FRP-to-concrete bonded joints. Compos Part B-Eng. 2015;70:64-79.

[28] Biscaia HC, Chastre C, Silva MA. Analytical model with uncoupled adhesion laws for the bond failure prediction of curved FRP-concrete joints subjected to temperature. Theor Appl Fract Mech. 2017;89:63-78.

[29] Zhou H, Torres JP, Fernando D, Law A, Emberley R. The bond behaviour of CFRP-to-steel bonded joints with varying bond properties at elevated temperatures. Eng Struct. 2019;183:1121-33.

[30] Deng J, Lee MMK, Moy SSJ. Stress analysis of steel beams reinforced with a bonded CFRP plate. Compos Struct. 2004;65:205-15.

[31] Stratford T, Cadei J. Elastic analysis of adhesion stresses for the design of a strengthening plate bonded to a beam. Constr Build Mater. 2006;20:34-45.

[32] Schnerch D, Dawood M, Rizkalla S, Sumner E. Proposed design guidelines for

strengthening of steel bridges with FRP materials. Constr Build Mater. 2007;21:1001-10.

[33] Dai JG, Ueda T, Sato Y. Development of the Nonlinear Bond Stress–Slip Model of Fiber Reinforced Plastics Sheet–Concrete Interfaces with a Simple Method. J Compos Constr. 2005;9:52-62.

[34] Yu T, Fernando D, Teng JG, Zhao XL. Experimental study on CFRP-to-steel bonded interfaces. Compos Part B-Eng. 2012;43:2279-89.

[35] Yuan H, Lu X, Hui D, Feo L. Studies on FRP-concrete interface with hardening and softening bond-slip law. Compos Struct. 2012;94:3781-92.

[36] Yuan H, Teng JG, Seracino R, Wu ZS, Yao J. Full-range behavior of FRP-to-concrete bonded joints. Eng Struct. 2004;26:553-65.

[37] Wang JL. Cohesive zone model of intermediate crack-induced debonding of FRP-plated concrete beam. Int J Solids Struct. 2006;43:6630-48.

[38] De Lorenzis L, Zavarise G. Cohesive zone modeling of interfacial stresses in plated beams. Int J Solids Struct. 2009;46:4181-91.

[39] Zhou H, Gao WY, Biscaia HC, Wei XJ, Dai JG. Debonding analysis of FRP-to-concrete interfaces between two adjacent cracks in plated beams under temperature variations. Eng Fract Mech. 2022;263.

[40] Guo D, Gao WY, Dai JG. Effects of temperature variation on intermediate crack-induced debonding and stress intensity factor in FRP-retrofitted cracked steel beams: An analytical study. Compos Struct. 2021:114776.

[41] Guo D, Gao WY, Fernando D, Dai JG. Effect of temperature variation on the plate-end debonding of FRP-strengthened beams: A theoretical study. Adv Struct Eng. 2021; 279:114776.[42] Camanho PP, Davila CG, de Moura MF. Numerical simulation of mixed-mode progressive delamination in composite materials. J Compos Mater. 2003;37:1415-38.

[43] Cui W, Wisnom M, Jones M. A comparison of failure criteria to predict delamination of unidirectional glass/epoxy specimens waisted through the thickness. Composites. 1992;23:158-66.

[44] Wu EM, Reuter Jr R. Crack extension in fiberglass reinforced plastics. University of Illinois, 1965.

[45] Benzeggagh ML, Kenane M. Measurement of mixed-mode delamination fracture toughness of unidirectional glass/epoxy composites with mixed-mode bending apparatus. Compos Sci and Technol. 1996;56:439-49.

[46] Fernando ND. Bond behaviour and debonding failures in CFRP-strengthened steel members: The Hong Kong Polytechnic University; 2010.

[47] Teng JG, Fernando D, Yu T. Finite element modelling of debonding failures in steel beams flexurally strengthened with CFRP laminates. Eng Struct. 2015;86:213-24.

[48] Deng J, Li JH, Wang Y, Xie WZ. Numerical study on notched steel beams strengthened by CFRP plates. Constr Build Mater. 2018;163:622-33.

[49] De Lorenzis L, Fernando D, Teng JG. Coupled mixed-mode cohesive zone

modeling of interfacial debonding in simply supported plated beams. Int J Solids Struct. 2013;50:2477-94.

[50] He J, Xian G, Zhang YX. Effect of moderately elevated temperatures on bond behaviour of CFRP-to-steel bonded joints using different adhesives. Constr Build Mater. 2020;241:118057.

[51] Li N, Li S, Liu C, Zhu T. Bond Behavior of CFRP/Steel Double Strap Joint at Elevated Temperatures. Preprints 2018.[52] Smith ST, Teng JG. Interfacial stresses in plated beams. Eng Struct. 2001;23:857-71.

[53] Dai JG, Ueda T, Sato Y. Unified analytical approaches for determining shear bond characteristics of FRP-concrete interfaces through pullout tests. J Adv Concr Technol. 2006;4:133-45.

[54] Abaqus V. 6.14 Documentation. Dassault Systemes Simulia Corporation. 2014.

[55] Dai JG, Gao WY, Teng JG. Finite element modeling of insulated FRP-strengthened RC beams exposed to fire. J Compos Constr. 2015;19:04014046.

[56] Gao WY, Dai JG, Teng JG. Simple method for predicting temperatures in insulated, FRP-strengthened RC members exposed to a standard fire. J Compos Constr. 2015;19:04015013.

[57] Gao WY, Dai JG, Teng JG. Fire resistance design of un-protected FRP-strengthened RC beams. Mater Struct. 2016;49:5357-71.

[58] Gao WY, Dai JG, Teng JG. Three-level fire resistance design of FRP-strengthened RC beams. J Compos Constr. 2018;22:05018001.

[59] Zhang L, Teng JG. Finite element prediction of interfacial stresses in structural members bonded with a thin plate. Eng Struct. 2010;32:459-71.